JGR Atmospheres

RESEARCH ARTICLE
10.1029/2024JD041458

Assimilation of Radar Reflectivity Data Using Parameterized Forward Operators for Improving Short-Term Forecasts of High-Impact Convection Events

Peng Liu[1,2], Jidong Gao[3], Guifu Zhang[1,2], and Jacob T. Carlin[3]

[1]School of Meteorology, University of Oklahoma, Norman, OK, USA, [2]Advanced Radar Research Center, University of Oklahoma, Norman, OK, USA, [3]NOAA/OAR National Severe Storms Laboratory, Norman, OK, USA

Key Points:

- The impacts of assimilating radar reflectivity using newly developed parameterized forward operator (PFO) are evaluated for real cases
- The PFO improved the analysis results compared to conventional Rayleigh-scattering-approximation-based forward operator (RFO)
- The PFO produced better forecasts of reflectivity and hourly precipitation with smaller biases than RFO

Supporting Information:

Supporting Information may be found in the online version of this article.

Correspondence to:

P. Liu,
Peng.Liu-1@ou.edu

Citation:

Liu, P., Gao, J., Zhang, G., & Carlin, J. T. (2024). Assimilation of radar reflectivity data using parameterized forward operators for improving short-term forecasts of high-impact convection events. *Journal of Geophysical Research: Atmospheres*, *129*, e2024JD041458. https://doi.org/10.1029/2024JD041458

Received 25 APR 2024
Accepted 27 SEP 2024

Author Contributions:

Conceptualization: Peng Liu, Jidong Gao
Investigation: Peng Liu, Jidong Gao, Jacob T. Carlin
Methodology: Peng Liu, Jidong Gao, Guifu Zhang
Project administration: Guifu Zhang
Validation: Peng Liu
Visualization: Peng Liu
Writing – original draft: Peng Liu
Writing – review & editing: Peng Liu, Jidong Gao, Guifu Zhang, Jacob T. Carlin

Abstract The assimilation of radar reflectivity requires an accurate and efficient forward operator that links the model state variables to radar observations. In this study, newly developed parameterized forward operators (PFO) for radar reflectivity with a new continuous melting model are implemented to assimilate observed radar data. To assess the impact of the novel parameterized reflectivity forward operators on convective storm analysis and forecasting, two distinct sets of cycled assimilation and forecast experiments are conducted. One set of experiments (ExpRFO) uses a conventional Rayleigh-scattering-approximation-based forward operator (RFO) with hydrometeor classification, while the other uses the PFO (ExpPFO_New) for radar reflectivity with a new continuous melting model. Eight high-impact severe convective weather events from the Hazardous Weather Testbed (HWT) 2019 Spring Experiments are selected for this study. The analysis and forecast results are first examined in detail for a classic tornadic supercell case on 24 May 2019, with the potential benefits provided by the PFO then evaluated for all eight cases. It is demonstrated that ExpPFO_New provides more robust results in terms of improving the short-term severe weather forecasts. Compared to ExpRFO, ExpPFO_New better reproduces all observed supercells in the analysis field, yields a more continuous and reasonable reflectivity distribution near the melting layer, and improves the strength of the cold pool compared to observations. Overall, ExpPFO_New, initialized from the more accurate analysis fields, produces better forecasts of reflectivity and hourly precipitation with smaller biases, especially at heavy precipitation thresholds.

Plain Language Summary The efficient and effective ingestion of radar reflectivity observations into convection-resolving models is critical because reflectivity provides explicit information about hydrometeors within thunderstorms, revealing their development and evolution. Therefore, accurate formulas that link what models predict and what radars observe are required. In this study, a new set of more-accurate formulas has been implemented and tested for several high-impact thunderstorm events and compared to the conventional formulas. We find that analyses derived using these new formulas more accurately depict the precipitation melting process and improve the prediction of thunderstorms in terms of intensity, location, and precipitation amount.

1. Introduction

Convective-scale numerical weather prediction (NWP) of high-impact severe weather events that produce flash flooding, damaging winds, hail, tornadoes, and lightning and their attendant socioeconomic impacts remains challenging in many regards. Among the primary challenges is the lack of accurate initial conditions that can fully represent detailed storm structures. Weather radar networks can provide high temporal and spatial resolution radar observations, such as radar reflectivity in horizontal polarization (Z_h in mm^6 m^{-3} or Z_H in dBZ), radial velocity (v_r), and polarimetric variables, which contain rich information on precipitation microphysics. Over the past few decades, the assimilation of reflectivity using cloud analysis (Auligné et al., 2011; Hu et al., 2006), physical initialization (Yang et al., 2006), latent heat nudging (Stephan et al., 2008), three/four-dimension variational (3DVAR/4DVAR) methods (Gao et al., 2004; Gao & Stensrud, 2012; Sun & Wang, 2013; Wang et al., 2013a, 2013b; Xiao et al., 2007), ensemble Kalman filtering (EnKF) methods (Dowell et al., 2011; Tong & Xue, 2005; Yussouf et al., 2013; Zhang et al., 2004), or the hybrid EnKF and variational method (Gao & Stensrud, 2014; Liu et al., 2008) has led to impressive achievements in updating the dynamical and hydrometeor information for the model initial fields to improve convective storm forecasting.

Since radar reflectivity is a measurement of the power scattered by hydrometeors, a radar forward operator linking the model state variables to radar observations is necessary when assimilating reflectivity. The forward operators used in variational assimilation with tangent linear and adjoint models must be differentiable and efficient. Assuming the Marshall-Palmer distribution of raindrop sizes, Sun and Crook (1997) proposed assimilating reflectivity through the relation between the reflectivity, Z_h, and the mixing ratio of rain (q_r) and tested it in simulated experiments using the 4DVAR method. Subsequently, this Z_h–q_r relation was used to assimilate reflectivity in the 3DVAR and 4DVAR data assimilation system of the Weather Research and Forecasting (WRF) model, showing a positive impact in numerous real convective weather events (Lin et al., 2021; Wang et al., 2013a, 2013b; Xiao & Sun, 2007). However, this usefulness of the Z_H–q_r relation is limited due to the neglect of ice-phase particles.

To effectively assimilate reflectivity data and capture the intricate details of convective storms in the initial field, it is necessary to develop a reflectivity forward operator which considers the contribution of ice-phase particles, particularly in the context of deep moist convection. Gao and Stensrud (2012) addressed this by developing a reflectivity forward operator that includes three hydrometeor species (rain, snow, and hail/graupel), classified based on a background temperature field. Initially implemented in a 3DVAR assimilation framework, this forward operator was later extended to a hybrid three-dimensional ensemble-variational (3DEnVAR) data assimilation system (Gao & Stensrud, 2014). Assimilating reflectivity using this forward operator across different assimilation frameworks demonstrated improvements in the analysis and forecasting of convective storms (Chen et al., 2021; Hu et al., 2023; Liu et al., 2021; Pan et al., 2018). However, all forward operators based on the Rayleigh scattering approximation may be inadequate when applied to particles with an equivolume diameter greater than one-sixteenth of the radar wavelength, especially for liquid and mixed-phased hydrometeors with larger dielectric constants. Additionally, a hydrometeor classification scheme that depends on the background temperature may lead to reflectivity discontinuities near the specified temperature layer due to artificially arbitrary classifications and inaccurate calculations of reflectivity for the melting species.

Wang and Liu (2019) introduced a reflectivity forward operator designed to consider mixed-phase particles. This operator builds upon the melting model integrated into the polarimetric radar operator developed by Jung et al. (2008). Its implementation in the WRF data assimilation system (WRFDA) yielded an analysis that closely matched the observed reflectivity in terms of pattern and intensity. However, some challenges surfaced, particularly in instances where reflectivity is observed, but zero or very small values for model hydrometeors exist. In addition, the computation of numerous coefficients posed efficiency concerns for the operator.

In contrast to variational methods, the EnKF method, proven successful in numerous high-dimensional, nonlinear, and non-Gaussian data assimilation applications, allows for the assimilation of radar data using more complex forward operators. Based on the calculations for reflectivity of rain and ice particles by Smith et al. (1975) and Smith (1984), using the assumptions of the Lin-Gilmore microphysics scheme (Gilmore et al., 2004; Lin et al., 1983), Tong and Xue (2005) used the EnKF method to assimilate simulated reflectivity to update hydrometeor variables (rain, snow, and hail-graupel) in an idealized case study. Following a similar approach, Aksoy et al. (2009, 2010) and Dowell et al. (2011) assimilated observed reflectivity using the EnKF method to improve the analysis and forecasts for real cases. Unlike the Gao and Stensrud (2012) reflectivity operator, they employed a simpler method wherein snow is considered to have a wet (dry) surface when the temperature is above (below) freezing (i.e., 0°C). Another development in this domain is the Efficient Modular VOlume scanning RADar Operator (EMVORADO) by Zeng et al. (2016), designed for simulating reflectivity and radial velocity. EMVORADO was subsequently implemented for assimilating reflectivity using the EnKF method in the Consortium of Small-scale Modeling (COSMO) model (Bick et al., 2016; Gastaldo et al., 2021). In addition, the forward operator originally designed for polarimetric radar data assimilation by Jung et al. (2008, 2010) has also been used to assimilate reflectivity in variety of studies (Park et al., 2023; Putnam et al., 2019, 2021; Tong et al., 2020).

While the EnKF method excels at assimilating reflectivity with more complex and accurate forward operators compared to the variational method, it does come with certain limitations. These include a higher computational cost, potential ensemble collapse, and a low rank of the ensemble covariance matrix leading to spurious long-range correlations. Sensitivity to the selected ensemble samples is another drawback. Therefore, the variational method is widely employed in operational assimilation systems for its simplicity and efficiency. Despite its advantages, current radar forward operators in variational assimilation systems often rely on assumed intercept

parameters, presenting issues when dealing with melting or mixed-phase particles due to the Rayleigh approximation. To address these challenges, Zhang et al. (2021) developed a set of parameterized forward operators (PFOs) for polarimetric radar data in which radar variables were fitted to rigorous scattering calculations performed using the T-matrix method for cloud droplets, cloud ice, rain, snow, graupel, hail, and mixed-phase particles. Du et al. (2021) evaluated these PFOs for assimilating polarimetric radar data in a variational assimilation approach for an idealized case, reducing the root mean square errors (RMSEs) of model state variables at each analysis cycle. In the PFOs, a melting model was used to simulate melting particles (such as melting snow) because most bulk microphysics schemes neglect melting particles. Liu et al. (2024) proposed a new melting model implemented in the PFOs to enhance the representation of the melting layer. However, whether the new PFOs, which excel in the simulation of radar variables, can also have advantages in data assimilation and forecast experiments has not been explored so far and needs to be investigated and evaluated.

In this study, we assess the impact of assimilating reflectivity using the newly developed PFO in a 3DVAR framework on short-term severe weather forecasts for eight high-impact convective events and compare them to forecasts using a commonly used reflectivity forward operator based on the Rayleigh scattering approximation and hydrometeor classification (RFO) (Gao & Stensrud, 2012). Our goal is to investigate whether and how the assimilation of reflectivity with PFO can help improve the analyses and forecasts of these convective severe weather events. The assimilation system settings are detailed in Section 2, including the configuration of the 3DVAR assimilation system and the specifications of the radar forward operators. Section 3 describes the experimental design, model configuration, and the data used for assimilation and validation. Section 4 focuses on the evaluation of the analysis and forecasting results. Conclusions are summarized along with a discussion regarding future work in Section 5.

2. Assimilation System Setting

2.1. The 3DVAR Assimilation System

In this study, we employed the 3DVAR assismilation system following the approach outlined by Gao et al. (1999, 2004). This system, developed for convective-scale data assimilation, has been used at the Center for Analysis and Prediction of Storms (CAPS) and the National Severe Storms Laboratory (NSSL) for many years (Gao, 2017; Hu et al., 2023). The 3DVAR method aims to obtain optimal estimation of the analysis state by minimizing the cost function:

$$J(\mathbf{x}) = \frac{1}{2}\left(\mathbf{x}-\mathbf{x}^b\right)^T\mathbf{B}^{-1}\left(\mathbf{x}-\mathbf{x}^b\right) + \frac{1}{2}[H(\mathbf{x})-\mathbf{y}^o]^T\mathbf{R}^{-1}[H(\mathbf{x})-\mathbf{y}^o] + J_c(\mathbf{x}), \quad (1)$$

where $\mathbf{x}$ and $\mathbf{x}^b$ are the analysis or control and background vector, $\mathbf{B}$ and $\mathbf{R}$ are the background and observation error covariance metrics, respectively, H is the nonlinear forward operator for observation data, and $\mathbf{y}^o$ is the observation vector. The term $J_c(\mathbf{x})$ is the penalty or weak constraint term; a divergence equation constraint was used here. The basic analysis vector comprises six variables, including the wind components (u, v, and w), potential temperature (θ), pressure (p), and water vapor mixing ratio (q_v). In addition, the hydrometeor analysis vector includes six variables: the mass mixing ratios of cloud droplets (q_c), cloud ice (q_i), rainwater (q_r), snow (q_s), graupel (q_g), and hail (q_h). To alleviate the high nonlinearity of the radar reflectivity forward operator and accelerate minimization of the cost function, a power transformation function is applied to the q_v and six hydrometeor variables following Yang et al. (2020) and Hu et al. (2023).

2.2. Forward Operators for Radar Data

In an assimilation system, the forward operator H is used to transform the model state variables in model space to the observed variables in observation space. Reflectivity and radial velocity are assimilated in this study. The forward operator for v_r is described in Gao and Stensrud (2012) as follows:

$$v_r = u\sin\phi\cos\mu + v\cos\phi\cos\mu + w\sin\mu, \quad (2)$$

where μ is the elevation angle and ϕ is the azimuth angle of the radar beam, and u, v, and w are the zonal, meridional, and vertical components of the wind, respectively.

The radar reflectivity for horizontal polarization Z_H represented in decibels (dBZ) is as follows:

$$Z_H = 10 \log (Z_h). \tag{3}$$

The radar reflectivity factor Z_h ($mm^6\ m^{-3}$) is the sum of each species $Z_h(x)$:

$$Z_h = \sum Z_h(x), \tag{4}$$

where $x \in (c, i, r, s, g, h)$ represents cloud droplets, cloud ice, rain, snow, graupel, and hail, respectively. The forward operator developed by Gao and Stensrud (2012) with temperature-based hydrometeor classification includes only three hydrometeor species (rain, snow, and graupel/hail), where graupel and hail are combined into a single species. In contrast, the parameterized forward operators developed by Zhang et al. (2021) incorporate six hydrometeor species (c, i, r, s, g, h).

2.2.1. Rayleigh-Scattering-Approximation-Based Forward Operator (RFO) With Hydrometeor Classification

The forward operator developed by Gao and Stensrud (2012) for the assimilation of reflectivity follows a power-law relation and uses a background temperature for automatic hydrometeor classification. Based on the Rayleigh scattering approximation, if the background temperature is higher than 5°C, the reflectivity factor of rain $Z_h(r)$ ($mm^6\ m^{-3}$) can be given as follows:

$$Z_h(r) \approx Z_r = 11.25 \times 4^3 \times 10^{18} \times \left(\frac{1}{N_{0,r}}\right)^{3/4} \times \left(\frac{\rho_a q_r}{\pi \rho_r}\right)^{7/4}, \tag{5}$$

where ρ_a (kg m^{-3}) and q_r (kg kg^{-1}) are the air density and mixing ratio of rain, respectively. When the intercept parameter is assumed to be $N_{0,r} = 8 \times 10^6$ in m^{-4} and $\rho_r = 1000$ in kg m^{-3}, Equation 5 becomes $Z_h(r) = 3.63 \times 10^9 \times (\rho_a q_r)^{1.75}$. This is equivalent to the Z_h–q_r relation derived by Sun and Crook (1997). If the background temperature is lower than −5°C, the reflectivity of dry snow is calculated as follows:

$$Z_h(s) \approx \frac{|K_i|^2}{|K_w|^2}\left(\frac{\rho_s}{\rho_r}\right)^2 Z_s = 0.23 \times \left(\frac{\rho_s}{\rho_r}\right)^2 \times 11.25 \times 4^3 \times 10^{18} \times \left(\frac{1}{N_{0,s}}\right)^{3/4} \times \left(\frac{\rho_a q_s}{\pi \rho_s}\right)^{7/4}, \tag{6}$$

where K_i ($|K_i|^2 = 0.21$) and K_w ($|K_w|^2 = 0.93$) are the dielectric constant factors of ice and water, respectively. $\frac{|K_i|^2}{|K_w|^2}\left(\frac{\rho_s}{\rho_r}\right)^2$ is an approximation for the ratio of the dielectric constant factor between snow and water, which should be more rigorously represented by $\frac{|K_s|^2}{|K_w|^2}$, where $K_s = (\varepsilon_s - 1)/(\varepsilon_s + 2)$ and ε_s is the relative permittivity of snow, calculated from mixing formulas such as the Maxwell-Garnett formulas (Maxwell-Garnett, 1904). When $N_{0,s} = 3 \times 10^6$ in m^{-4} and $\rho_s = 100$ in kg m^{-3}, as is commonly assumed in bulk microphysics schemes, Equation 6 becomes $Z_h(s) = 9.80 \times 10^8 \times (\rho_a q_s)^{1.75}$. For hail, the reflectivity is calculated as follows:

$$Z_h(h) \approx \frac{|K_i|^2}{|K_w|^2}\left(\frac{\rho_h}{\rho_r}\right)^2 Z_h = 0.23 \times \left(\frac{\rho_h}{\rho_r}\right)^2 \times 11.25 \times 4^3 \times 10^{18} \times \left(\frac{1}{N_{0,h}}\right)^{3/4} \times \left(\frac{\rho_a q_h}{\pi \rho_h}\right)^{7/4}. \tag{7}$$

When $N_{0,h} = 4 \times 10^4$ in m^{-4} and $\rho_h = 900$ in kg m^{-3}, Equation 7 becomes $Z_h(h) = 4.33 \times 10^{10} \times (\rho_a q_h)^{1.75}$. If the background temperature lies between −5°C and 5°C, rain, hail, and wet snow are assumed to coexist. Using the dielectric constant of water as that of wet snow, the reflectivity factor for wet snow can be given as follows:

$$Z_h(s) \approx Z_s = 11.25 \times 4^3 \times 10^{18} \times \left(\frac{1}{N_{0,s}}\right)^{3/4} \times \left(\frac{\rho_a q_s}{\pi \rho_s}\right)^{7/4}. \tag{8}$$

Table 1
Summary of Selected Cases for Data Assimilation and Forecast Experiments

Date	Primary affected states	Hazardous weather	Convective event description
1 May 2019	TX, OK	Tornado, hail	A multi-cell thunderstorm
6 May 2019	TX, OK, KS	Damaging wind, hail	Isolated to widely scattered severe thunderstorms
20 May 2019	TX, OK, KS	Tornado, hail	Tornadic supercell
21 May 2019	MO, AR	Tornado, hail	A mixed mode of storms including supercells and bowing line
22 May 2019	OK, KS, MO	Tornado, hail	Clusters of supercells
23 May 2019	TX, OK, KS	Tornado, hail	A cluster of strong storms
24 May 2019	TX, OK, KS	Tornado, hail	Clusters of supercells
28 May 2019	KS, MO, IA, IL	Tornado, hail	Isolated supercell, mesoscale convective complex

After substituting the presumed values for $N_{0,s}$ and ρ_s, Equation 8 becomes $Z_h(s) = 4.26 \times 10^{11} \times (\rho_a q_s)^{1.75}$. Since the Rayleigh scattering approximation is valid only for particles that are spherical with sizes much smaller than the radar wavelength ($D < \lambda/16$), these power-law operators will be flawed when calculating the reflectivity contribution of large particles such as large hailstones and mixed-phase particles (Zhang, 2016). The treatment of applying the dielectric constant of water as that of wet snow, or determining wet snow based on the background temperature, also leads to a reflectivity discontinuity and inaccuracies near the melting layer.

2.2.2. Parameterized Forward Operator (PFO) With a New Continuous Melting Model

The PFOs for polarimetric radar data establish accurate and efficient relations between polarimetric radar variables and model state variables by deriving fits to robust T-matrix scattering calculations (Zhang et al., 2021). For the purposes of this study, only the PFO for radar reflectivity is utilized for assimilation.

For rain, $Z_h(r)$ is fitted to polynomial functions of mass/volume-weighted mean diameters (D_m, mm), as shown in Mahale et al. (2019):

$$Z_h(r) \approx W\left(-0.3078 + 20.87D_{m,r} + 46.04D_{m,r}^2 - 6.403D_{m,r}^3 + 0.2248D_{m,r}^4\right)^2, \tag{9}$$

where $W = \rho_a q_r$ in g m^{-3} is the liquid water content and q_r is in g kg^{-1}. For an exponential particle size distribution (PSD), the D_m (mm) can be defined using PSD moments as follows:

$$D_{m,x} \equiv \frac{M_{4x}}{M_{3x}} = \frac{4}{\Lambda} = 4\left(\frac{10^3 \rho_a q_x}{\pi \rho_x N_{t,x}}\right)^{1/3} = 4\left(\frac{10^3 \rho_a q_x}{\pi \rho_x N_0}\right)^{1/4}, \tag{10}$$

where Λ (mm^{-1}) is the slope parameter and N_0 (m^{-3} mm^{-1}) is the intercept parameter, the hydrometeor density is ρ_x (g cm^{-3}), mixing ratio is q_x (g kg^{-1}), and number concentration is $N_{t,x}$ (m^{-3}).

For a given melting species, the percentage of melting (f_{mx}), mixing ratio, number concentration, and density of the melting species are estimated in a continuous melting model (Liu et al., 2024). Then, the D_m is calculated from Equation 10, and the reflectivity factor $Z_h(x)$ (mm^6 m^{-3}) is parameterized as a polynomial function of D_m and f_{mx} as follows:

$$Z_h(x) \approx Z_x\left[a_{Z0}\left(f_{mx}\right) + a_{Z1}\left(f_{mx}\right)D_{m,x} + a_{Z2}\left(f_{mx}\right){D_{m,x}}^2 + a_{Z3}\left(f_{mx}\right){D_{m,x}}^3\right]^2, \tag{11}$$

where a_Z are fitting coefficients detailed in Tables 1 of Zhang et al. (2021). Z_x is the 6th moment of the PSD as follows:

$$Z_x \equiv M_{6x} = 11.25 \times 10^3 \frac{\rho_a q_x}{\pi \rho_x} {D_{m,x}}^3, \tag{12}$$

where the factor of 10^3 comes from the unit conversion as ρ_x is in g cm^{-3}, while D_m is in mm. By substituting D_m of Equation 10 into Equation 12, the following equation for Z_x is obtained:

$$Z_x = 11.25 \times 10^3 \times 4^3 \times \left(\frac{1}{N_0}\right)^{3/4} \times \left(\frac{\rho_a q_x}{\pi \rho_x}\right)^{7/4}. \quad (13)$$

When fixed values of N_0 and ρ_x typical of single-moment (SM) microphysics schemes (Gilmore et al., 2004; Lin et al., 1983) are used, Equation 13 reduces to Equations 5–8. Compared to Equation 11, Equation 13 clearly demonstrates the inaccuracies due to the Rayleigh approximation in the RFO.

Due to most bulk microphysics schemes failing to simulate melting hydrometeors, a melting model is used to generate melting particles in the radar forward operators. Liu et al. (2024) proposed a new melting model to estimate the mixing ratio and number concentration of melting species based on the geometric mean of rain and dry species. In comparison to the melting model used in the original PFO by Zhang et al. (2021), this new melting model allows for continuous changes in state parameters and radar reflectivity and provides more reasonable estimates for mixing ratios and number concentrations of melting hydrometeor species and is easier to linearize. In the melting model, the total mixing ratios q_{mx} and number concentration $N_{t,mx}$ of the melting species x are assumed to be

$$q_{mx} = \left(q_r q_x\right)^{1/2}, \quad (14)$$

$$N_{t,mx} = \left(N_{t,r} N_{t,x}\right)^{1/2}. \quad (15)$$

The percentage of melting f_{mx} (also called the mass water fraction) is given as follows:

$$f_{mx} = q_r/\left(q_r + q_x\right). \quad (16)$$

The mixing ratio of water ($q_{mx,r}$) and dry ice ($q_{mx,d}$) within the melting species are defined as follows:

$$q_{mx,r} = q_{mx} f_{mx} = \frac{q_{mx} q_r}{\left(q_r + q_x\right)}, \quad (17)$$

$$q_{mx,d} = q_{mx}\left(1 - f_{mx}\right) = \frac{q_{mx} q_x}{\left(q_r + q_x\right)}. \quad (18)$$

Following Jung et al. (2008), the density of the melting species, ρ_{mx}, is parameterized as follows:

$$\rho_{mx} = \rho_{dx}\left(1 - {f_{mx}}^2\right) + \rho_r {f_{mx}}^2, \quad (19)$$

where ρ_{dx} is the density of dry snow, hail, and graupel. More detail of the melting model can be found in Liu et al. (2024).

3. Experimental Design and Data

3.1. Experimental Design

In this study, eight real cases with severe convection events (01, 06, 20, 21, 22, 23, 24, and 28 May 2019, see Table 1) are chosen from the 2019 National Oceanic and Atmospheric Administration (NOAA) Hazardous Weather Testbed (HWT) Spring experiments (Clark et al., 2020). These cases are used to assess the impact of assimilating radar reflectivity with the PFO on short-term severe weather forecasts.

Two distinct sets of assimilation experiments are conducted. The first set, referred to as ExpRFO, utilizes the Rayleigh-scattering-approximation-based forward operator with hydrometeor classification developed by Gao and Stensrud (2012), as detailed in Section 2.2.1. This forward operator is also employed in the Warn-on-Forecast-Hybrid (WoF-Hybrid) system for assimilating radar reflectivity (Carpenter, 2022; Gao & co-authors, 2021). The second set, labeled ExpPFO_New, employs the PFO for radar reflectivity developed by

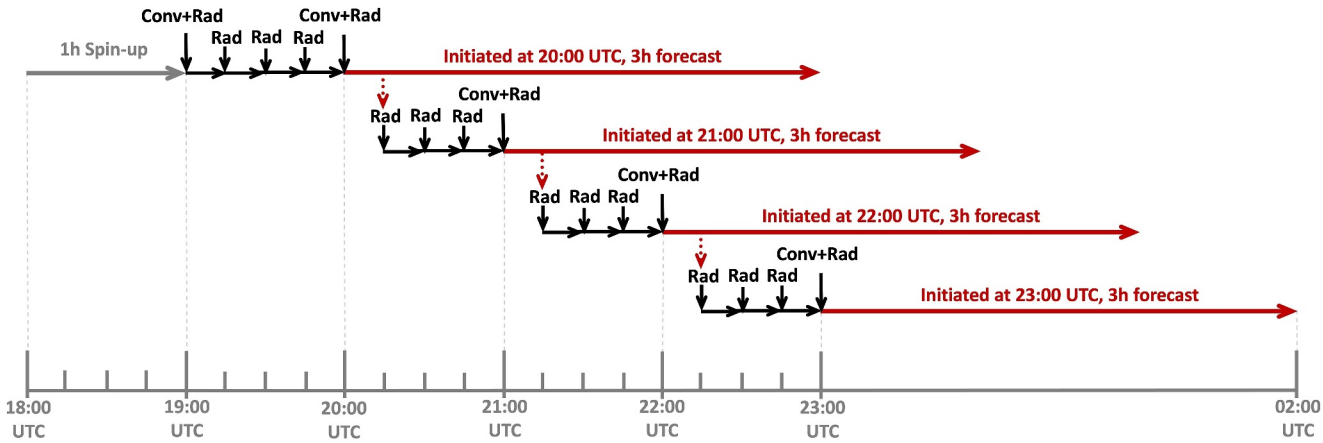

Figure 1. Flowchart of the cycled data assimilation and forecast experiments. Conventional observations (Conv) and radar observations (Rad) are assimilated in 1-hr and 15-min intervals, respectively.

Zhang et al. (2021) with a new continuous melting model by Liu et al. (2024), as explained in Section 2.2.2. In addition, an extra experiment (ExpPFO_4species) was conducted with the same settings as ExpPFO_New but without cloud water and cloud ice to assess the impact of the additional species included in the PFO for one convection case. The flowchart of the cycled data assimilation and forecast experiments is depicted in Figure 1. For all eight cases, the model was initialized at 1800 UTC each day. After a 1-hr spin-up period, the first data assimilation began at 1900 UTC, followed by cycled data assimilation in 15-min intervals until 2300 UTC with 3-hr forecasts initiated at the top of the hour (2000, 2100, 2200, and 2300 UTC respectively).

In our analysis and forecast experiments, the WRF model version 3.7.1 (Skamarock et al., 2008) is utilized as the forecast model. The model domain is configured with 601 × 601 grid points with a 1.5-km horizontal grid spacing, while the vertical dimension comprises 51 eta levels, extending up to a model top at 50 hPa. The initial and boundary conditions are obtained from the 3.0-km High-Resolution Rapid Refresh (HRRR) forecast product at 1-hr intervals (Dowell et al., 2022). The physics parameterization schemes we used include the Milbrandt-Yau double-moment microphysics scheme (Milbrandt and Yau, 2005a, 2005b), the Rapid Radiative Transfer Model for General Circulation Models (RRTMG) for both long-wave and short-wave radiation schemes (Iacono et al., 2008), the unified Noah land surface model, and the Yonsei University planetary boundary layer physics scheme (Hong et al., 2006). No cumulus parameterization scheme is employed.

3.2. Observational Data for Assimilation and Validation

For each case, the assimilated radar data includes radial velocity and reflectivity, while conventional observations include data from surface stations, buoys, and soundings. All radar data are obtained from the NEXRAD Level-II data repository at the National Centers for Environmental Information (NOAA, 2015). Prior to assimilation, the raw radar data from Volume Coverage Patterns (VCPs) undergo quality control. This involves radial velocity de-aliasing, removal of radar ground clutter, and elimination of non-meteorological and outlier reflectivity gates. After quality control, radar data are linearly interpolated onto the model grid. In cases where reflectivity from multiple radars exists at a model point, the largest reflectivity value is chosen.

The performance of the analyses and forecasts in this study is verified using composite radar reflectivity, surface observations from the Oklahoma Mesonet (Brock et al., 1995) and Automated Surface/Weather Observing Systems (ASOS), and the National Centers for Environmental Prediction (NCEP) Stage-IV hourly precipitation data set. Before validation, observed radar reflectivity and precipitation data are linearly interpolated onto the model grid. To obtain an accurate reflectivity simulation for comparison with observation, the PFO is used to calculate the analyzed and forecast reflectivity for all experiments.

4. Results

To illustrate the impact of assimilating radar reflectivity with the newly developed PFO on short-term severe weather forecasts, a detailed investigation of the 24 May case is first presented in Sections 4.1 and 4.2. The choice

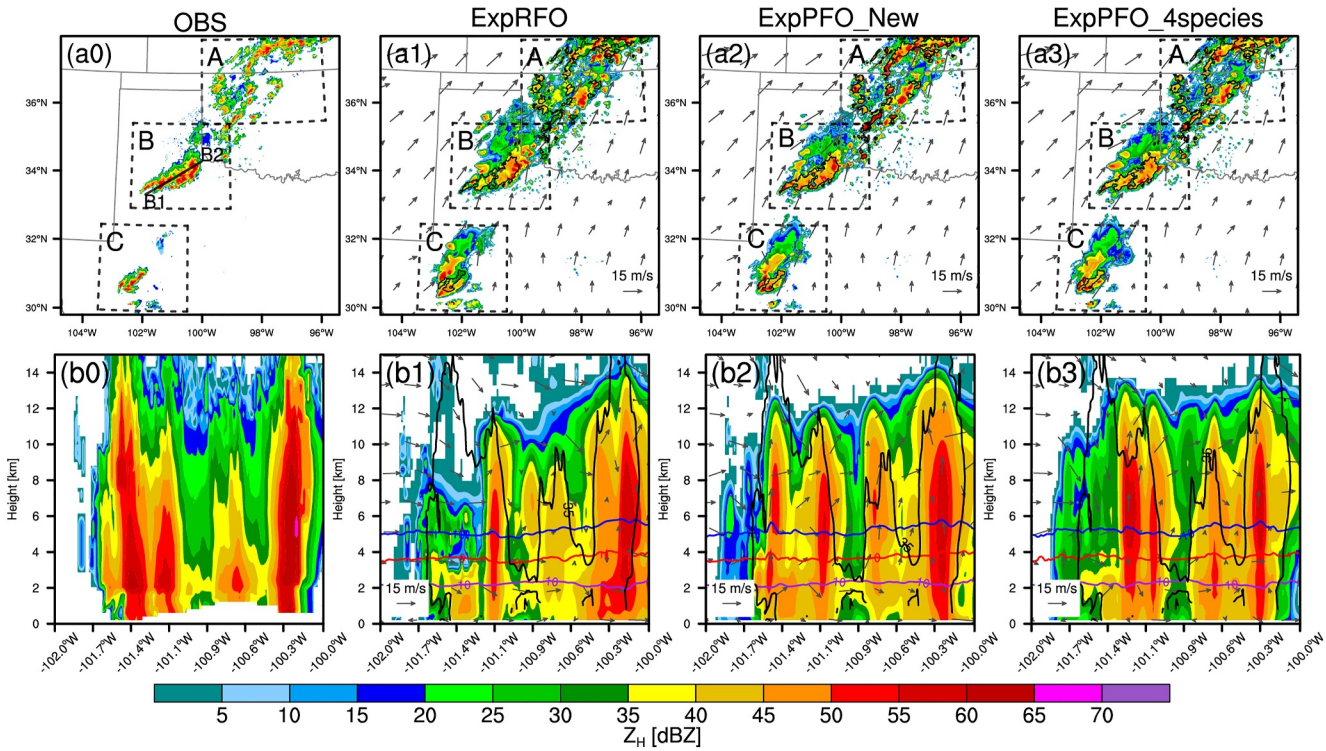

Figure 2. Horizontal cross-sections (a0–a3) at $z = 3.0$ km and vertical-sections (b0–b3) of observed (a0 and b0) and analyzed (a1–b3) reflectivity at 2200 UTC on 24 May 2019. Panels (a1, b1) display the analysis results from ExpRFO using the Rayleigh-scattering-approximation-based forward operator with hydrometeor classification (RFO). Panels (a2, b2) and (a3, b3) display the results from ExpPFO_New and ExpPFO_4species using the parameterized forward operators for radar reflectivity (PFO) included and without cloud water and ice, respectively. The black solid line in panels (a1–b3) represents observed reflectivity contours (35 dBZ). The black dashed rectangular box (A, B, and C) denotes the domain used for analysis and computation of the contoured frequency by the altitude diagram (CFAD) in the later section. In panel (a0), the black line (B1–B2) indicates where vertical cross-sections are taken. In vertical-section panels, the 10°C (purple line), 0°C (red line), and −10°C (blue line) isotherms are shown in panels (b1–b3).

of the 24 May case is motivated by two reasons: it was one of the highest-impact severe weather events of 2019 with 183 severe weather reports including 19 tornadoes. Most of these reports occurred within our analysis and forecast domain, where high temporal and spatial resolution surface observations were available for verification. On this day, a cold front extended from southern Texas through northeast Kansas. An influx of very moist air with surface dewpoints around 21°C supported moderate to strong instability, and vertical wind profiles with 20–25 m s^{-1} effective bulk shear supported supercell development (SPC, 2019). Around 2300 UTC, a cluster of supercells in northwest Texas moved across parts of southwest Oklahoma, and strong to severe storms were observed from northern Oklahoma through eastern Kansas. Large hail, damaging wind gusts, and several tornadoes were reported in these areas. To gain an overall understanding of the usefulness of the new reflectivity forward operator, the aggregated evaluation of all eight severe weather events is shown in Section 4.3.

4.1. Analysis Results: 24 on May 2019

4.1.1. Reflectivity

The horizontal and vertical cross-section of reflectivity at 2200 UTC on 24 May 2019 from the cycled analysis of ExpRFO, ExpPFO_New, and ExpPFO_4species is compared against observed reflectivity in Figure 2. A cluster of convective cells are observed in northwest Oklahoma and southern Kansas (labeled Region A), well-developed multiple supercells exist in northwest Texas (labeled Region B), and another multicell convective storm is present in west Texas (labeled Region C). Overall, all three experiment analyses reproduce the observed convective cells and supercells. However, the intensity of convective cells in Region A and supercells in Region B in ExpRFO and ExpPFO_4species is significantly weaker than that in ExpPFO_New, which is closer to the observations (Figures 2a1–2a3). The vertical cross-section taken through the supercell cores in Region B allows a clearer comparison between three experiments (Figures 2b0–2b3). In the vertical cross-section, three supercells with

reflectivity exceeding 55 dBZ and echo tops close to 12 km are observed (Figure 2b0), but ExpRFO fails to reproduce the leftmost one (Figure 2b1). Notably, the model-predicted reflectivity values in ExpRFO are very clearly missing above the 0°C isotherm in comparison with the observations, indicating that inaccuracies in the description of larger particle reflectivity by RFO lead to a failure to reproduce all observed storms even after multiple cycling analyses. ExpPFO_4species also show a weaker analysis for the leftmost storm (Figure 2b3). Overall, ExpPFO_New greatly improved the analyzed reflectivity of supercells compared to ExpRFO, reproducing all observed supercells effectively (Figure 2b2).

Contoured Frequency by Altitude Diagrams (CFADs) provide a comprehensive representation of the distribution of reflectivity at different altitudes and are used to compare analysis results with observations. CFADs of the analyzed reflectivity at 2200 UTC are constructed for the regions indicated by the three black boxes A, B, and C in Figure 2a0. In Region A, the observed reflectivity increases continuously with decreasing altitude, reaching a maximum at 2 km AGL (Figure 3a0). In Regions B and C, where multiple supercells are present, the observed reflectivity reaches a maximum before reaching the surface, exceeding 55 dBZ (Figures 3b0 and 3c0). In all three regions, especially in Region A, ExpRFO shows jumps or discontinuities in reflectivity at about 4 km AGL near the −5°C isotherm compared to the observed CFADs (Figures 3a1–3c1). As mentioned in Section 2.2, the RFO achieves the effect of considering wet snow by increasing the dielectric constant, that is, the dielectric constant of water was used for wet snow. However, since hydrometeor classification is determined by the background temperature, for example, wet snow limited to between the −5°C and 5°C levels, it can easily lead to the issue of different dielectric constants being used for the same kind of particles in the calculation of reflectivity. This results in the discontinuity and inaccuracy of reflectivity near the melting layer. Additionally, the Rayleigh scattering approximation is not valid for larger particles. For example, there is an underestimation of the reflectivity based on the Rayleigh scattering approximation when the D_m of wet hail ($f_{mx} = 80\%$) is between 5 and 20 mm, while an overestimation is exhibited when the D_m of wet hail over 20 mm (see Figure 2a of Zhang et al., 2021). Consequently, the maximum reflectivity analyzed by ExpRFO is less than observed in all three regions.

The PFOs are based on the results of accurate T-matrix scattering calculations and moderate the issue of underestimation of the reflectivity of larger particles and overestimation of very large particles in the Rayleigh scattering approximation. Therefore, the reflectivity analyzed by ExpPFO_New and ExpPFO_4species is more accurate than that in ExpRFO and is closer to observations (Figures 3a2–3c3). ExpPFO_New and ExpPFO_4species employ a continuously varying melting model that is not directly dependent on the background temperature, resulting in a more continuous and smooth reflectivity distribution although reflectivity values are occasionally slightly larger than those observed. In essence, PFOs serve as fundamentally more accurate radar forward operators than those based on the Rayleigh scattering approximation. This is further evident in the real-case analysis results above. Compared with ExpPFO_4species, ExpPFO_New produces larger reflectivity near the ground, which is closer to observations. This indicates that the inclusion of cloud water and ice improves the analysis of reflectivity to some extent, despite not contributing significantly to reflectivity themselves.

4.1.2. Hydrometeors

In general, analysis results that yield reflectivity close to those observed imply a more reasonable distribution of hydrometeors. Figure 4 shows the vertical cross-section of analyzed mixing ratios for rain and ice particles from ExpRFO, ExpPFO_New, and ExpPFO_4species. The absence of ice-phase particles leads to the failure of the storm analysis on the far-left side of the vertical cross-section in ExpRFO. This aligns with findings reported in Liu et al. (2022), where the Rayleigh-scattering-approximation-based operator produces an overestimated rainwater mixing ratio and underestimated snow and hail mixing ratios. ExpPFO_New reproduces the leftmost storm well, primarily due to the adjustment of ice-phase particles, which results in more snow, graupel, and hail obtained at the storm locations.

4.1.3. Temperature and Dew Point Temperature at 2 m

Assimilating radar observations through variational approaches primarily updates the wind field and hydrometeors in the analysis field and does not directly adjust the storm environment. After multiple cycled analyses, differences in forward operators change microphysical processes through their effect on the adjustments of hydrometeors, which, in turn, affect the storm environment. The 2-m temperatures and dewpoint temperatures from Oklahoma Mesonet and ASOS observations and three experiments are shown in Figure 5. In Regions A and B, all

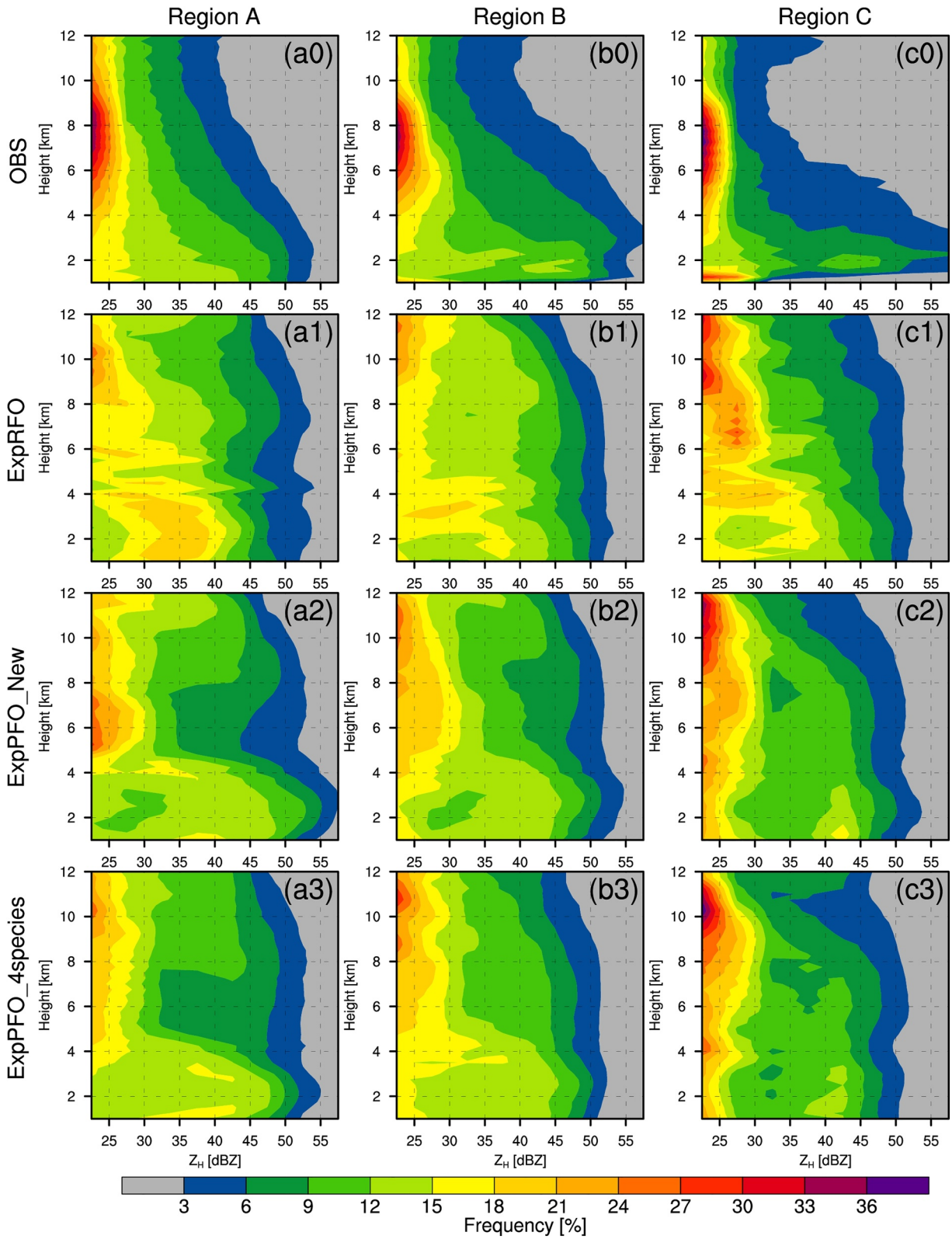

Figure 3. Contoured frequency by altitude diagrams (CFADs, %) of reflectivity (Z_H, dBZ) using observations (a0–c0) and analysis results from ExpRFO (a1–c1), ExpPFO_New (a2–c2), and ExpPFO_4species (a3–c3) within the black dashed rectangular boxes A (a0–a3), B (b0–b3), and C (c0–c3) in Figure 2 at 2200 UTC on 24 May 2019.

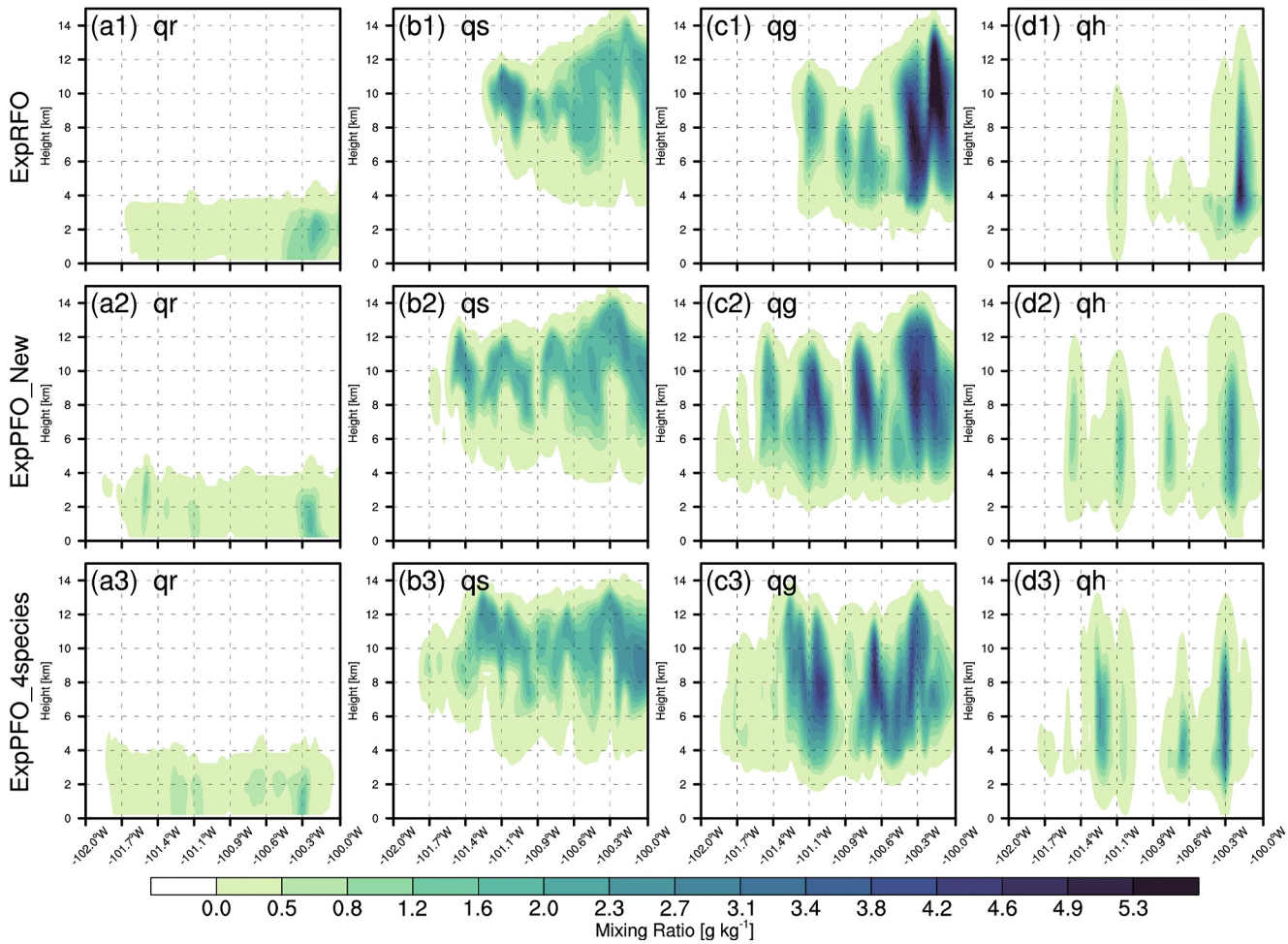

Figure 4. Vertical cross-sections of analyzed mixing ratios (g kg^{-1}) for rain (q_r) (a1–a3), snow (q_s) (b1–b3), graupel (q_g) (c1–c3), and hail (q_h) (d1–d3) at 2200 UTC on 24 May 2019, obtained from ExpRFO (a1–d1), ExpPFO_New (a2–d2), and ExpPFO_4species (a3–d3) along the line B1–B2 in Figure 2.

experiments show warmer and drier results than the observations (Figures 5a1–5a3, 5c1–5c3), suggesting there is a model error independent from the impacts of assimilation. Compared to ExpRFO, ExpPFO_New simulates lower temperatures in these areas, especially in Region B, where ExpPFO_New minus ExpRFO exhibits a temperature difference of more than 3°C (Figure 5b1). For the dew point temperature, the difference between ExpRFO and ExpPFO_New is smaller compared to the difference in simulated temperatures, indicating that ExpPFO_New has a smaller difference between the dew point and temperature than ExpRFO (Figure 5d1). In Region A, the dew point temperatures of ExpPFO_New and ExpRFO are very close to each other, suggesting that ExpPFO_New produces colder and wetter air at the surface, that is, a stronger cold pool, than ExpRFO. The strength of the cold pool influences the degree of convergence and is critical to the development and evolution of the storm.

4.2. Forecast Evaluation: 24 on May 2019

4.2.1. Reflectivity

Whether the advantage of the PFO in the analysis field carries over to benefit short-term forecasts is examined in this section. An example of the forecast reflectivity field from ExpRFO, ExpPFO_New, and ExpPFO_4species for the 3-hr forecast initiated at 2200 UTC, and the corresponding observations are shown in Figure 6. At 2300 UTC, 1 hr into the forecast, the results with ExpPFO_New successfully predict the mesoscale convective system (MCS) in northwest Texas, while the forecast with ExpRFO produces two split convective clusters (Figure 6a1, 6a2). At 0000 UTC, the observed reflectivity indicates that multiple supercells in northwest Texas merged with

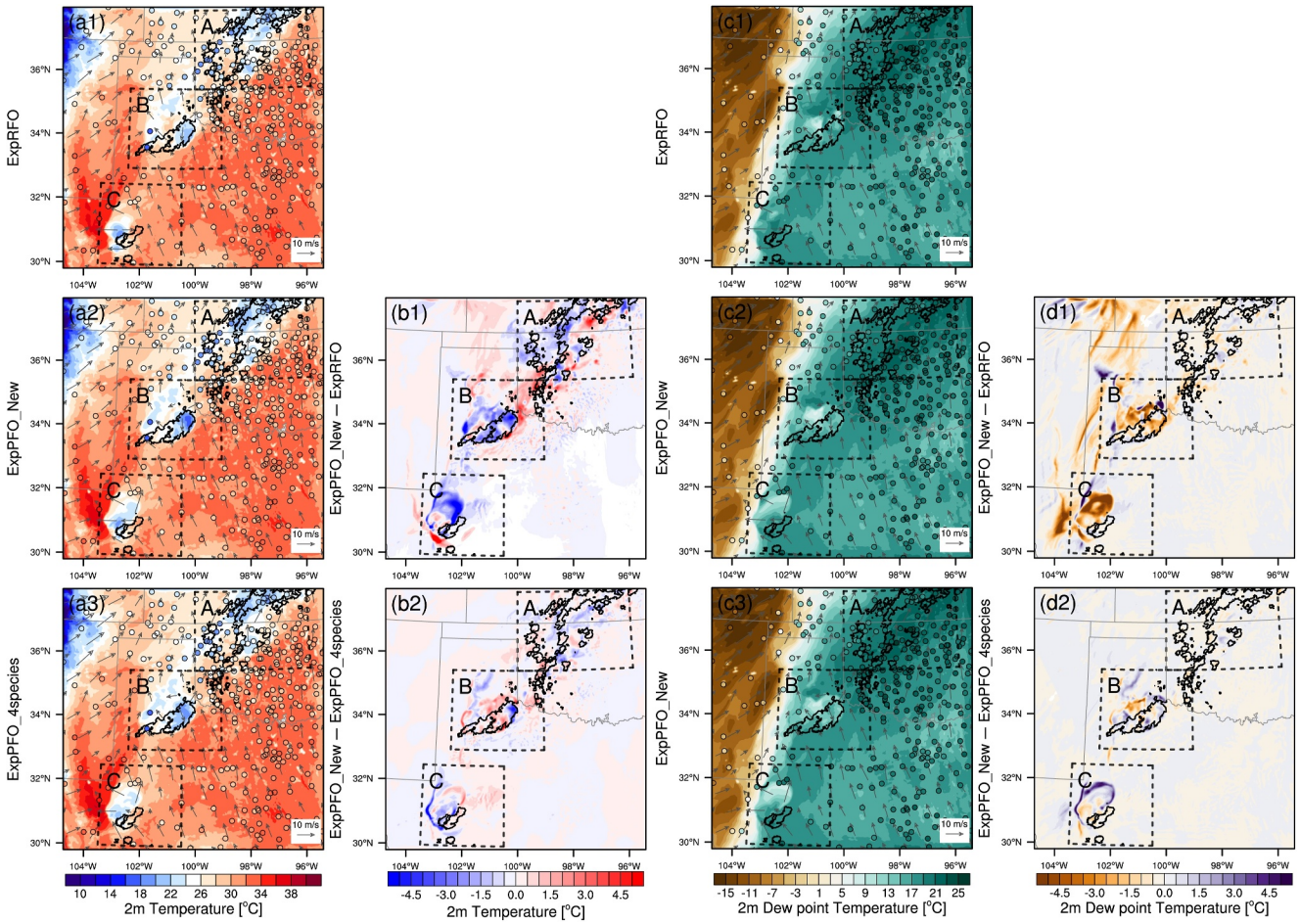

Figure 5. Comparison of 2-m temperature (a1–b2) and dew point temperature (c1–d2) from the observation (shaded circles, °C) and simulation (shading, °C) along with 10-m wind (arrows, m s^{-1}) from ExpRFO (a1, c1), ExpPFO_New (a2, c2), and ExpPFO_4species (a3, c3) at 2200 UTC on 24 May 2019. Panels (b1, d1) and (b2, d2) display the differences of ExpPFO_New minus ExpRFO and ExpPFO_New minus ExpPFO_4species, respectively. The black line represents observed reflectivity contours (35 dBZ) in panels (a1–d2).

clusters of convective cells in northwest Oklahoma to form an organized squall line (Figure 6b0). The forecasts of all experiments face challenges in reproducing the observed squall lines completely, but the forecasts with ExpPFO_New and ExpPFO_4species produce convective cells in slightly better agreement with the observations than ExpRFO (Figures 6b2, 6b3 vs. Figure 6b1).

To quantitatively evaluate the reflectivity forecast at different assimilation cycles, neighborhood equitable threat scores (NETS) and bias scores (NBIAS) with a 6-km radius at three reflectivity thresholds are calculated in Figures 7 and 8. Larger NETS values indicate higher forecast skill. For NBIAS, a value closer to 1 indicates a smaller bias. A value of NBIAS greater than 1 indicates that there are more false alarms than misses, and less than 1 indicates that there are more misses than false alarms (Clark et al., 2010). Overall, the NETSs of ExpPFO_New and ExpPFO_4species are greater than that of ExpRFO at different thresholds in most assimilation periods (Figures 7e1–7e3). The most obvious improvement in reflectivity in ExpPFO_New compared to ExpRFO occurs within the first hour of the forecasts, with the improvement diminishing after 1 hour. Additionally, larger NETS values can be achieved after multiple cycles of assimilating radar data for all experiments. Correspondingly, NBIAS gradually approaches 1 and becomes greater than 1 after multiple cycles of assimilation (Figures 8d1–8d3). This may be due to phase errors and spurious cells existing in the forecast of all experiments.

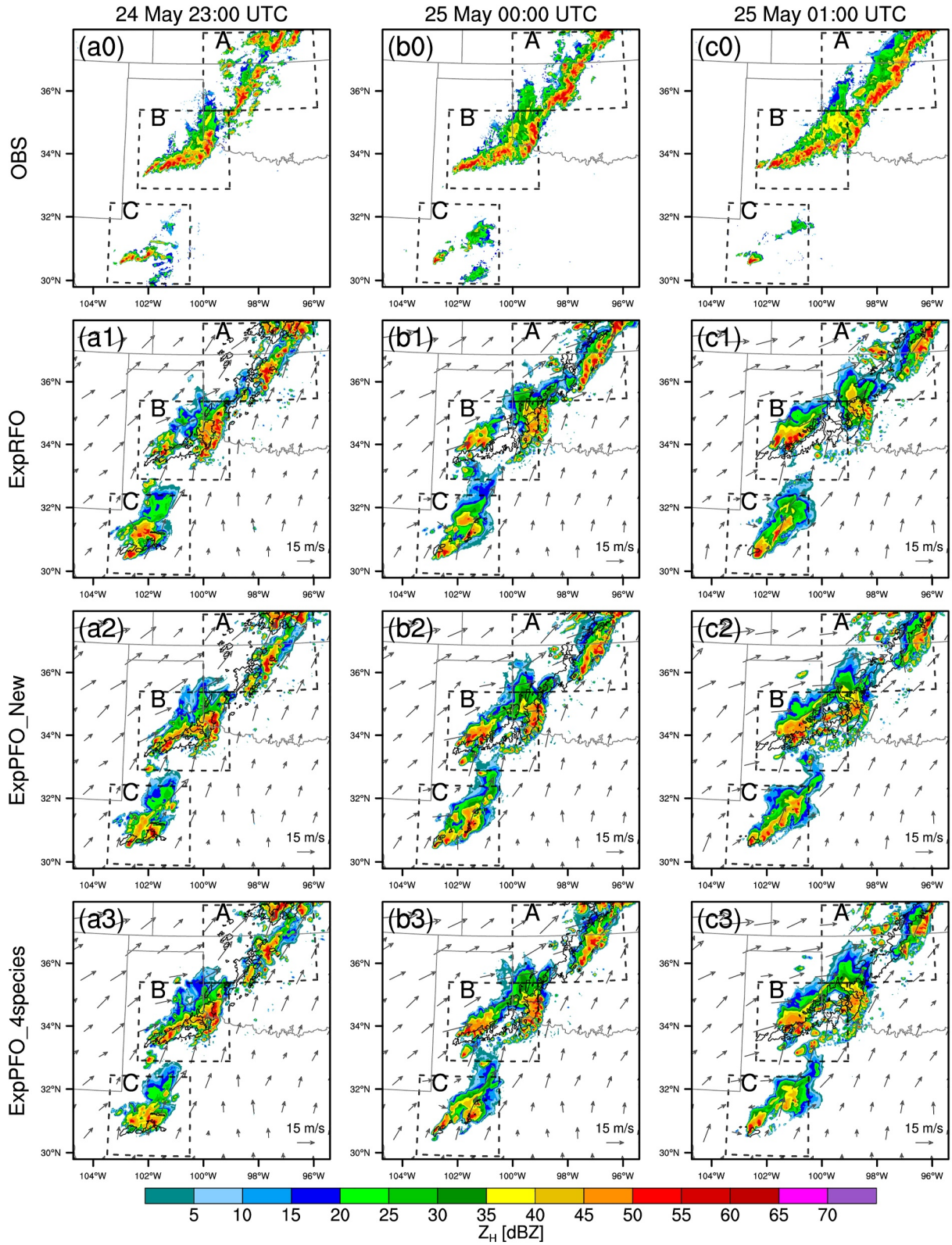

Figure 6. Horizontal cross-sections of observed (a0–c0) and forecasted (a1–c3) reflectivity (Z_H, dBZ) at z = 3.0 km at 2300 UTC on 24 May (a0–a3), 0000 UTC on 25 May (b0–b3), and 0100 UTC on 25 May (c0–c3) 2019. Panels (a1–c1), (a2–c2), and (a3–c3) display forecast results initiated at 2200 UTC from ExpRFO, ExpPFO_New, and ExpPFO_4species, respectively. The observed reflectivity contours (35 dBZ) are represented by black lines in panels (a1–c3).

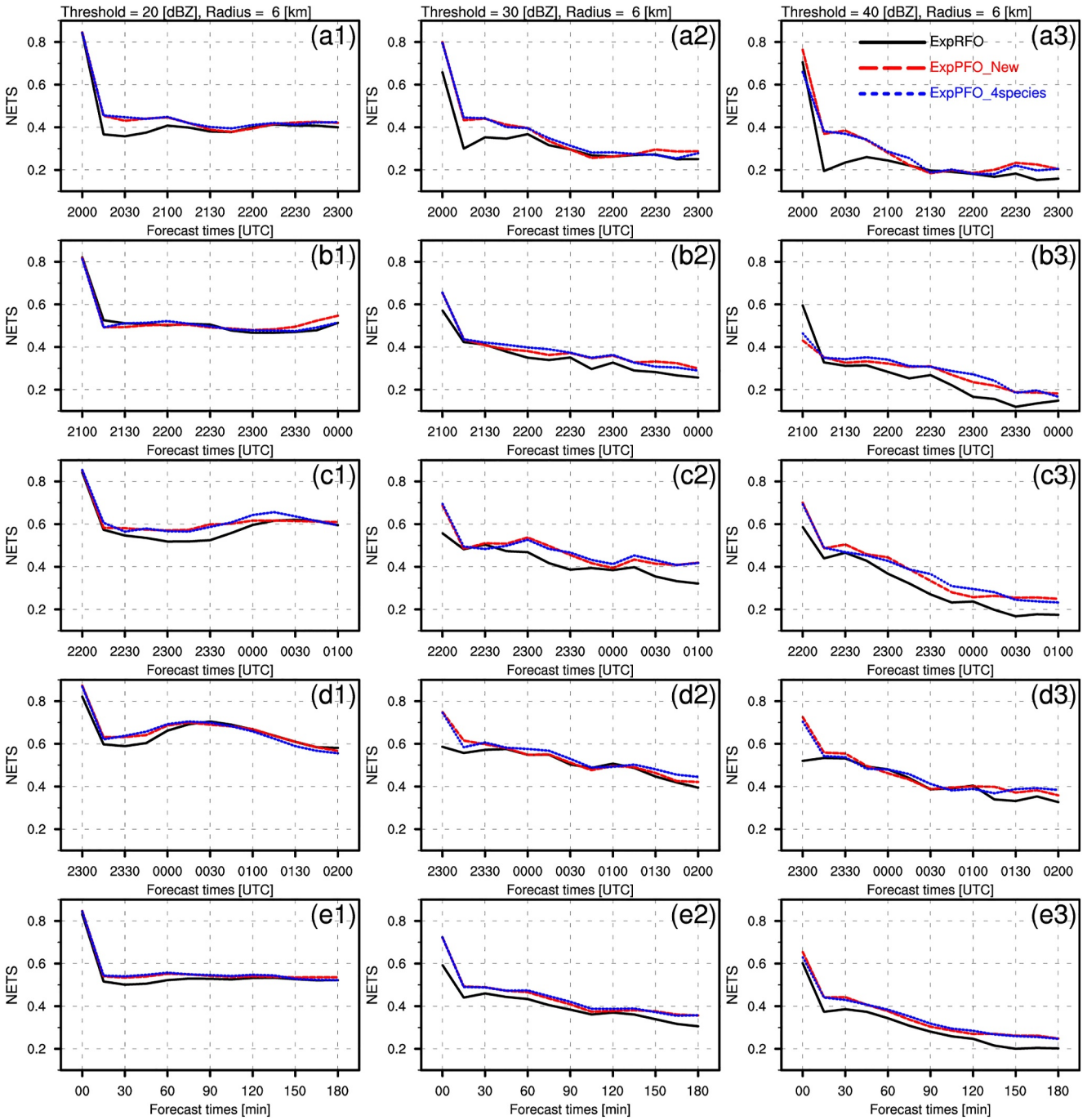

Figure 7. The neighborhood equitable threat score (NETS) with a 6-km radius for 0–3 hr composite reflectivity forecasts initiated at 2000 UTC (a1–a3), 2100 UTC (b1–b3), 2200 UTC (c1–c3), 2300 UTC (d1–d3), and averaged over four cycles (e1–e3) for reflectivity thresholds with 20 dBZ (a1–e1), 30 dBZ (a2–e2), and 40 dBZ (a3–e3). ExpRFO, ExpPFO_New, and ExpPFO_4species are represented by black solid lines, red, and blue dashed lines, respectively.

4.2.2. Precipitation

The 3-hr accumulated precipitation from the forecasts of all experiments initiated at 2200 UTC is further compared with observations in Figure 9. Two primary precipitation areas are observed in the model domain. One is a northeast-southwest-oriented band of precipitation from the MCS in northwest Texas that merged with a cluster of convective cells in northwest Oklahoma during its movement. The other is an isolated, relatively weak precipitation band located in west Texas. All experiments do a good job forecasting the shape and location of the

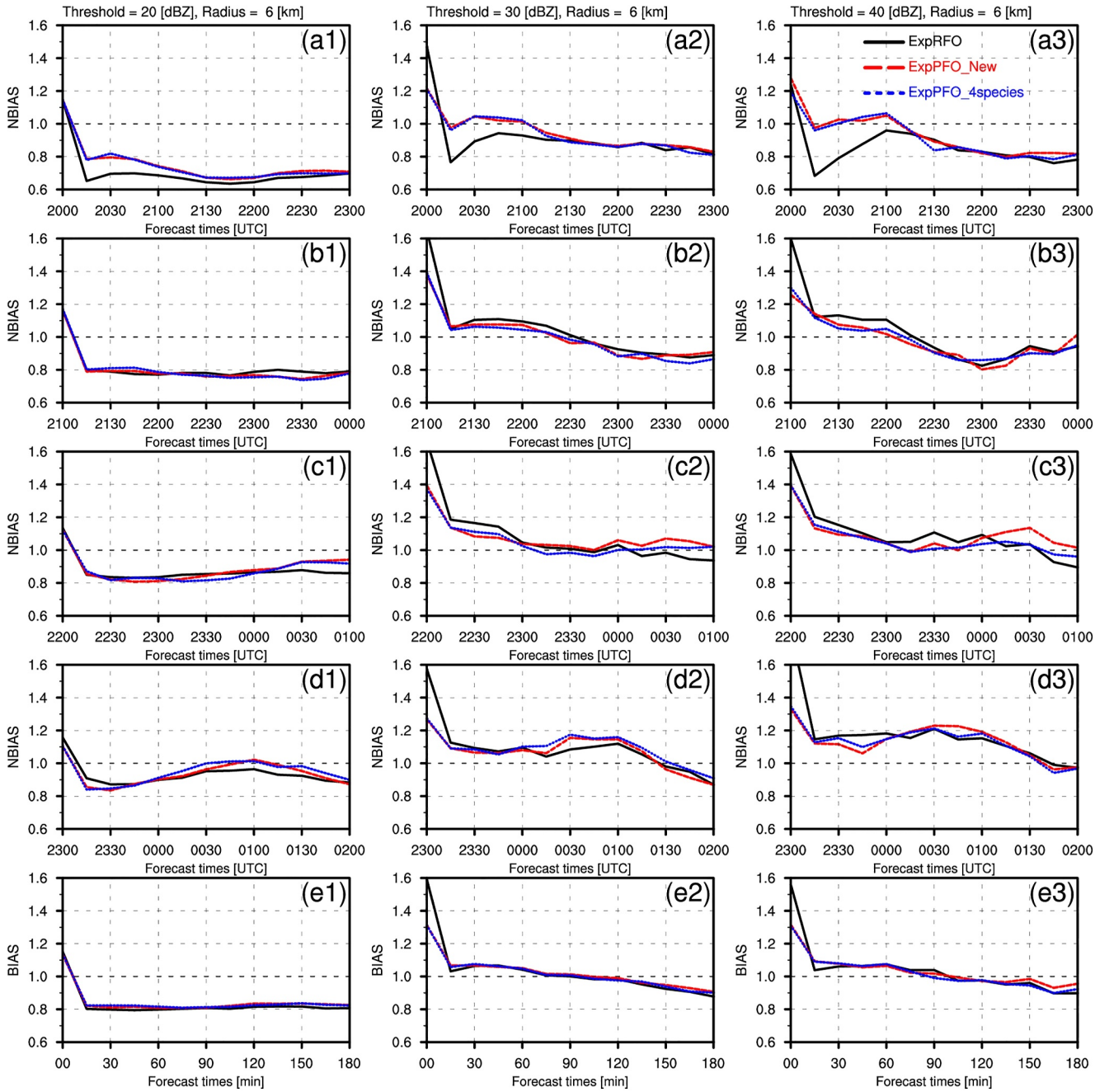

Figure 8. As in Figure 7, but for the neighborhood bias (NBIAS).

two main precipitation bands. For the precipitation band across Texas and Oklahoma, the ExpRFO underpredicts precipitation intensity with a northern bias compared to the observations (Figures 9a0, 9a1). ExpPFO_New and ExpPFO_4species improve the forecast of precipitation intensity by better matching the observations (Figures 9a2 and 9a3). For the precipitation band in west Texas, all experiments overforecast the precipitation amount compared to the observations, with ExpRFO showing the largest discrepancy.

The NETS and NBIAS with a 6-km radius for hourly precipitation at four thresholds are calculated to quantitatively evaluate the performance of all experiments. As shown in Figure 10, ExpPFO_New and ExpPFO_4species achieve higher NETS than ExpRFO at all thresholds, with more significant improvements for heavy precipitation ($\geq$10 mm hr^{-1}) (Figures 10e1–10e4). Notably, the improvement in precipitation forecasting by

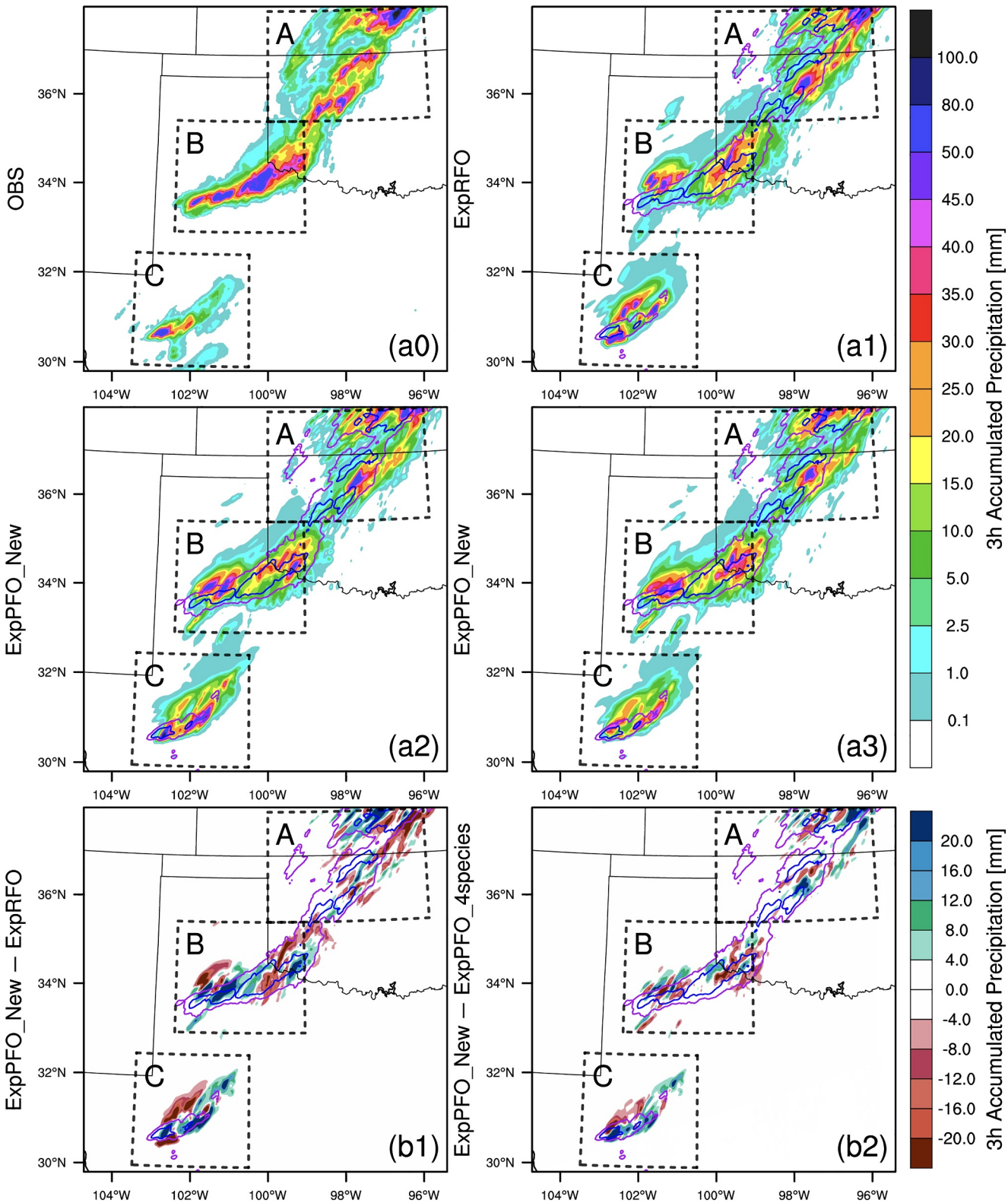

Figure 9. The 3-hr accumulated precipitation (shading, mm) from observations (a0) and forecasts (a1–a3) from ExpRFO, ExpPFO_New, and ExpPFO_4species initiated at 2200 UTC 24 May 2019. Panels (b1) and (b2) display the differences of ExpPFO_New minus ExpRFO and ExpPFO_New minus ExpPFO_4species, respectively. The observed 3-hr accumulated precipitation contours at 5 mm (purple lines) and 30 mm (blue lines) are shown in panels (a1–b2).

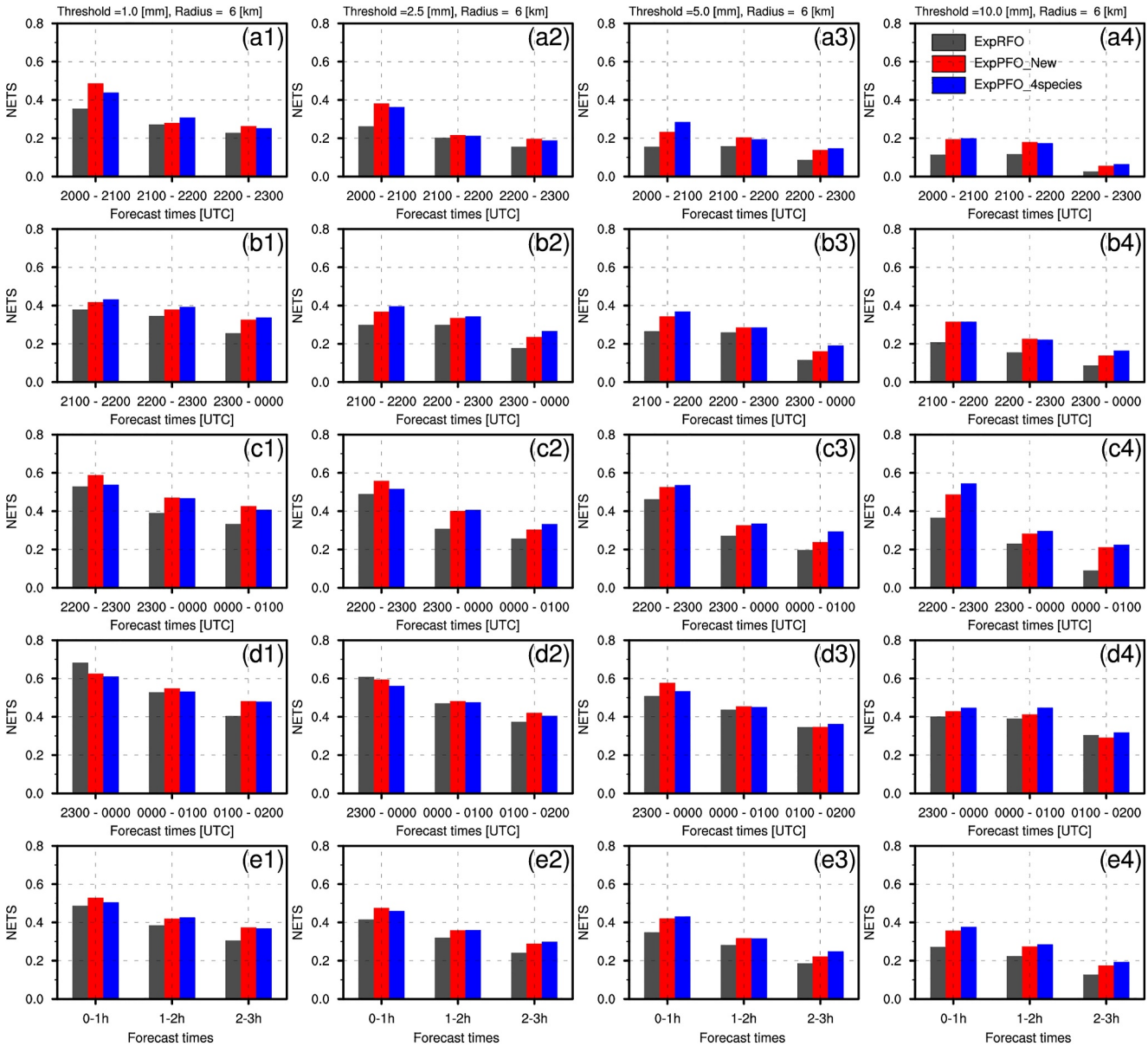

Figure 10. The neighborhood equitable threat score (NETS) with a 6-km radius for 1-hr accumulated precipitation forecasts initiated at 2000 UTC (a1–a4), 2100 UTC (b1–b4), 2200 UTC (c1–c4), 2300 UTC (d1–d4), and averaged over four cycles (e1–e4) for the precipitation threshold of 1.0 mm (a1–e1), 2.5 mm (a2–e2), 5.0 mm (a3–e3), and 10.0 mm (a4–e4). ExpRFO, ExpPFO_New, and ExpPFO_4species are represented by gray, red, and blue bars, respectively.

ExpPFO_New and ExpPFO_4species is not only evident at the 1-hr forecast but also at the 2-hr and 3-hr forecasts. This is consistent with the analysis in Section 4.1.3. The assimilation of radar data using the PFO can better improve the distribution of hydrometeors in the analysis field, which, in turn, affects other model characteristics (e.g., cold pools), allowing the benefits on the analysis field to be consistently transferred to the forecasting of precipitation. ExpPFO_New and ExpPFO_4species are relatively close to each other, which suggests that the PFO can achieve higher NETS than the RFO without cloud water and ice.

For hourly precipitation, the mostly negative NBIAS values are gradually reduced with more data assimilation cycles and reach minimums (i.e., close to 1) when the forecasts are initialized from 2200 UTC (Figures 11a1–11c4). More positive biases can be seen from the forecast results with all experiments after four assimilation cycles, that is, initiated at 2300 UTC (Figures 11d1–11d4). Overall, the PFO significantly reduces the NBIAS of hourly precipitation at all thresholds, especially at the 1-hr forecast. However, all experiments have issues with

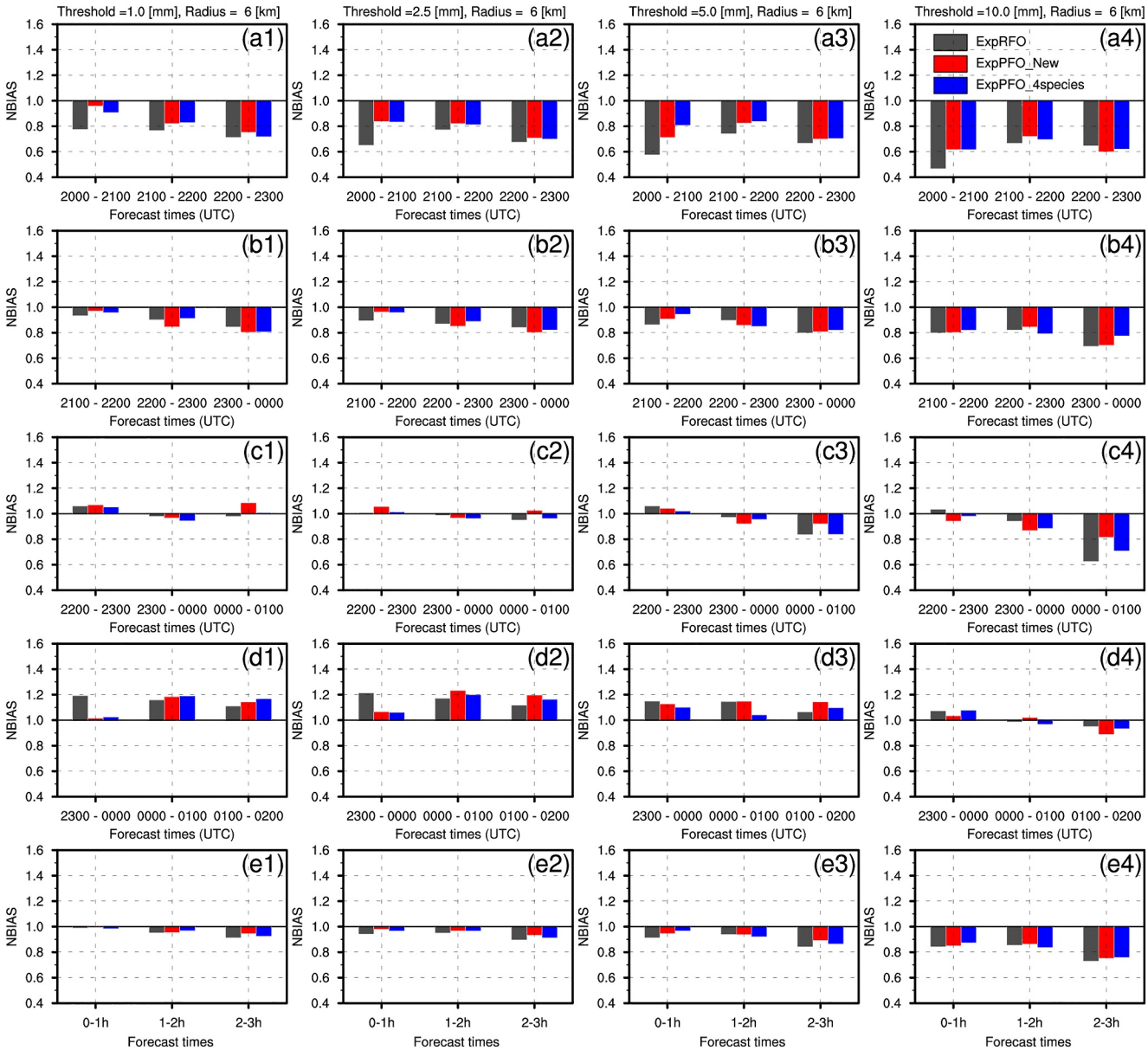

Figure 11. As in Figure 10, but for the neighborhood bias (NBIAS).

spurious precipitation, which is common when frequently assimilating radar data. Introducing more constraints, assimilating zero reflectivity, or other methods may alleviate this issue in variational assimilation (Gan et al., 2022; Li et al., 2023; Lin et al., 2021).

4.3. Evaluation Over All Eight Cases

The above exploration details the impact of the reflectivity PFO on the analysis and forecasts of the 24 May 2019 event. To provide a general picture about the performance of ExpPFO_New in comparison with ExpRFO, a quantitative evaluation of all eight severe convection events described in Section 3.1 and Table 1 is presented in this section.

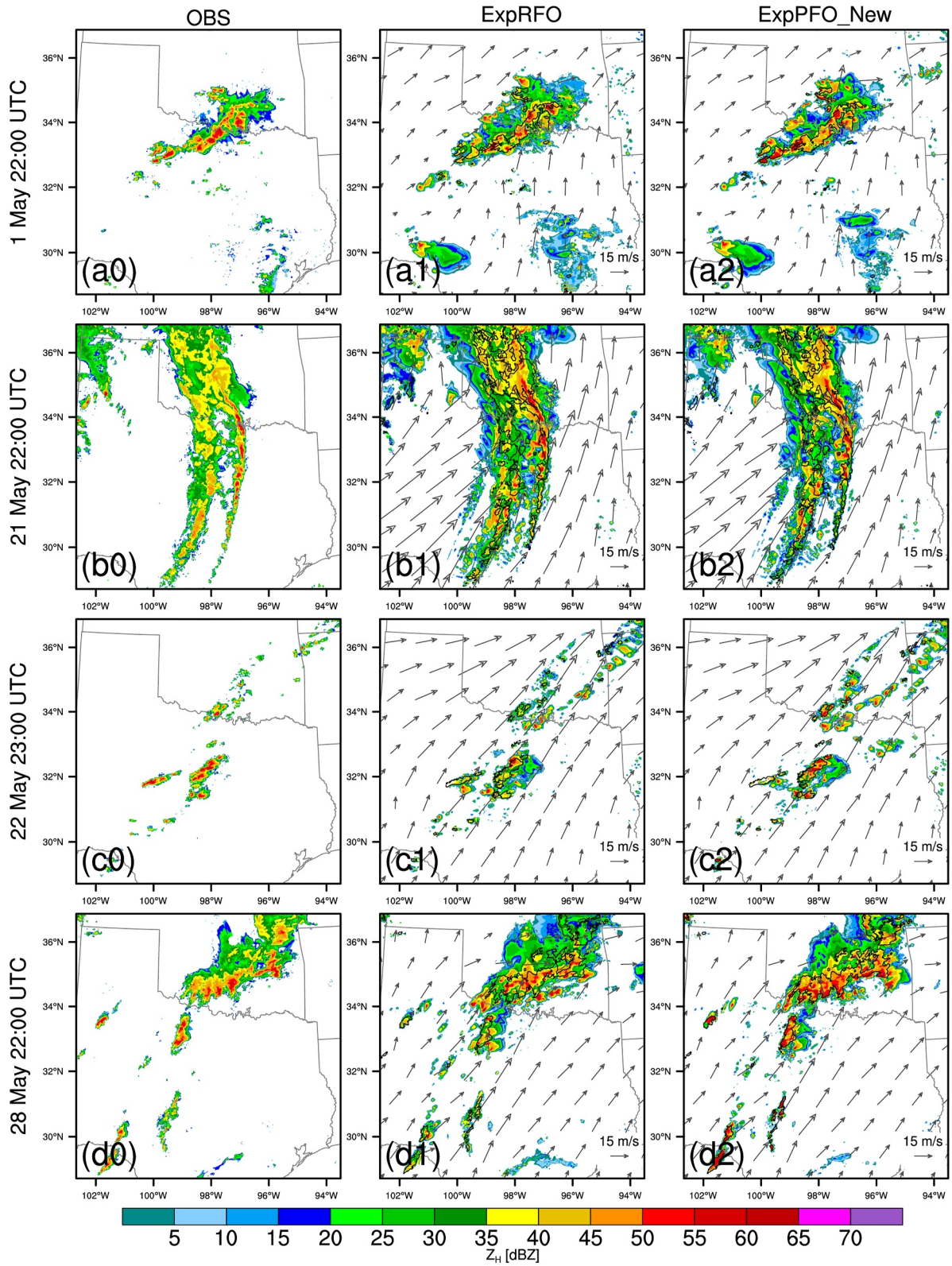

Figure 12. Horizontal cross-sections of observed (a0–d0) and analyzed (a1–d2) reflectivity at $z = 3.0$ km at 2200 UTC on 1 May (a0–a2), 2200 UTC on 21 May (b0–b2), 2300 UTC on 22 May (c0–c2), and 2200 UTC on 28 May (d0–d2) 2019. Panels (a1–d1) and (a2–d2) display the analysis results from ExpRFO and ExpPFO_New. The black solid line in panels (a1–d2) represents observed reflectivity contours (35 dBZ).

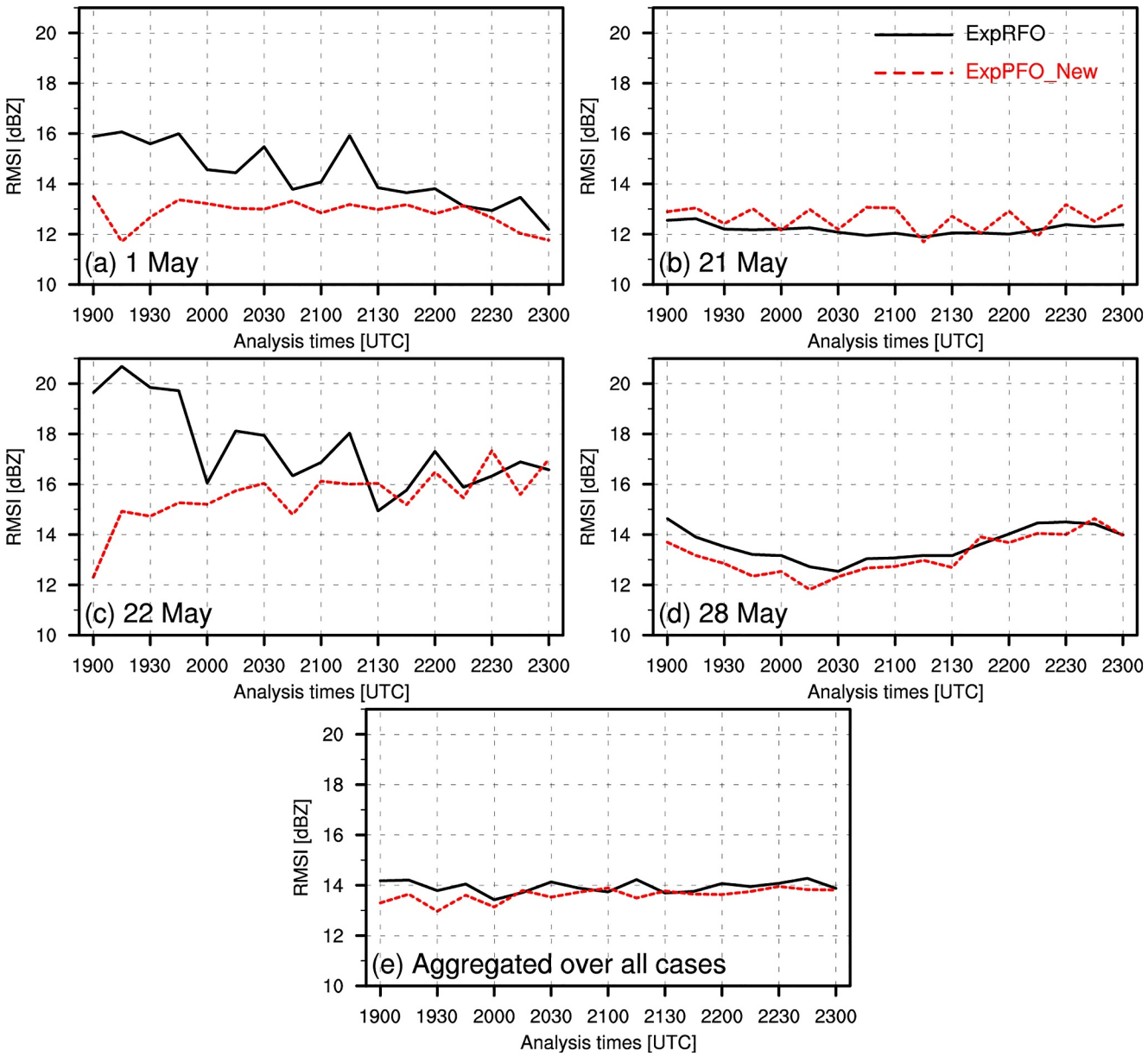

Figure 13. The Root mean square innovation (RMSI) for reflectivity (Z_H, dBZ) at 15-min intervals during the data assimilation period. Panels (a–d) display cases of 1 May, 21 May, 22 May, and 28 May 2019, respectively. Panel (e) displays the result of aggregated over all eight cases. ExpRFO and ExpPFO_New are represented by black solid lines and red dashed lines, respectively.

4.3.1. Analysis Results

The horizontal cross-section of observed and analyzed reflectivity for four cases is shown in Figure 12, and the other cases can be found in the Supporting Information S1. Multiple types of convective cases show that ExpPFO_New exhibits improved, closer-to-observation analysis of reflectivity than ExpRFO for cases of the clusters of supercells (1, 20, 22, 24, and 28 May), except for the insignificant improvement for a mixed mode of storms including supercells and squall lines (6, 21, and 23 May). The root mean square innovation (RMSI), which gives a measure of the overall distance between the observations and the analysis (Aksoy et al., 2010), is calculated for each case and averaged over all eight cases in Figure 13. Compared to ExpRFO, the ExpPFO_New unsurprisingly exhibits smaller averaged RMSI across most assimilation periods (Figure 13). With the same assimilation configuration, using the more accurate PFOs yields an analysis result that is more consistent with observations. The old forward operator which classifies hydrometeors based on background temperature

inevitably produces discontinuities and inaccuracies of reflectivity near the melting layer, such as the overestimation of reflectivity when treating dry snow as wet snow or the underestimation of reflectivity when treating wet snow that has not fully melted as dry snow. The PFOs with the continuous melting model certainly improve the discontinuity and inaccuracy of reflectivity near the melting layer.

4.3.2. Forecast Results

The NETS of each case and averaged over all cases for composite reflectivity from ExpRFO and ExpPFO_New at different thresholds are compared in Figure 14. At the 30-min forecast, the NETS of ExpPFO_New are better than those of ExpRFO, and then their difference gradually decreases with forecast time. After 1 hr, the NETS averaged over the eight cases of ExpRFO and ExpPFO_New nearly overlaps. The difficulty in sustaining improvements from the PFO beyond 1 hr may be related to significant model errors in the WRF model.

Figure 15 shows the NETS of hourly accumulated precipitation from ExpRFO and ExpPFO_New forecasts for each case and averaged over eight cases. The ExpPFO_New improved NETS for hourly accumulated precipitation at each threshold while reducing NBIAS (not shown), especially at the heavy precipitation threshold and in the first forecast hour. This is consistent with the results from the single case of 24 May 2019 previously described.

5. Conclusions and Discussion

This study investigates the impact of using newly developed parameterized forward operators (PFOs) for radar reflectivity with a new continuous melting model in the variational data assimilation framework on short-term severe weather forecasts. This new scheme is tested for eight high-impact convection events from HWT Spring Forecast Experiments. To assess the benefits of using PFOs for analysis and forecasting, a comparison is made with a widely used forward operator, which was developed based on the Rayleigh scattering approximation (RFO) with hydrometeor classification. An additional experiment using PFO but without cloud water and ice is performed to test the impact of the additional species. The study provides a detailed evaluation of the analysis and forecast results for a specific tornadic supercell case on 24 May 2019 in Texas, Oklahoma, and Kansas. Subsequently, the potential benefits of PFO are further assessed to offer a more comprehensive understanding of the improvement in short-term forecasts across all eight cases examined.

The experiments (ExpRFO) using the RFO have some shortcomings in accurately reproducing observed convective storms and supercells in the analysis field. This is attributed to inherent limitations in calculating radar reflectivity for large particles like hail and mixed-phase particles. Additionally, ExpRFO's reliance on background temperature for hydrometeor classification introduces discontinuities and inaccuracies in the analyzed reflectivity, particularly near the melting layer. The cumulative effect of these limitations after multiple assimilation cycles results in an underestimation of the cold pool strength in the analysis field. The experiments (ExpPFO_New) using the PFO demonstrate some improvements in the analyzed reflectivity, successfully reproducing all observed storms for the 24 May 2019 case. This success can be attributed to the improved accuracy of the PFO, which is based on T-matrix scattering calculations rather than the Rayleigh scattering approximation and better represents the reflectivity of large particles ($D > \lambda/16$). The new melting model incorporated in the PFO, which is not directly dependent on background temperature, contributes to a more continuous, smooth, and accurate distribution of reflectivity near the melting layer. The inclusion of cloud water and ice in the PFO affects the analysis results, but only to a relatively small extent. The enhanced distribution of hydrometeors by the PFO had a positive impact on strengthening the cold pool, resulting in improvements for short-term severe weather forecasts in terms of NETS and NBIAS for forecast reflectivity and hourly accumulated precipitation, particularly at heavy precipitation thresholds.

The overall improvement of ExpPFO across all eight cases is not as pronounced as in the single case of 24 May. However, it consistently yields the best forecast skills in the first hour for composite reflectivity and hourly accumulated precipitation forecasts at each threshold. The disappearance of the improvements with PFO in short-range forecasts beyond 1 hour may be due to significant model errors as well as the lack of balanced analysis for other model variables in the 3DVAR approach. This broader evaluation, including different convective events, provides more evidence for the superiority of PFOs over the forward operator based on the Rayleigh scattering approximation with hydrometeor classification. It should be clarified that the fundamental advantage of PFO lies in its more accurate calculation of the backscattering amplitudes for all species, including liquid and ice particles

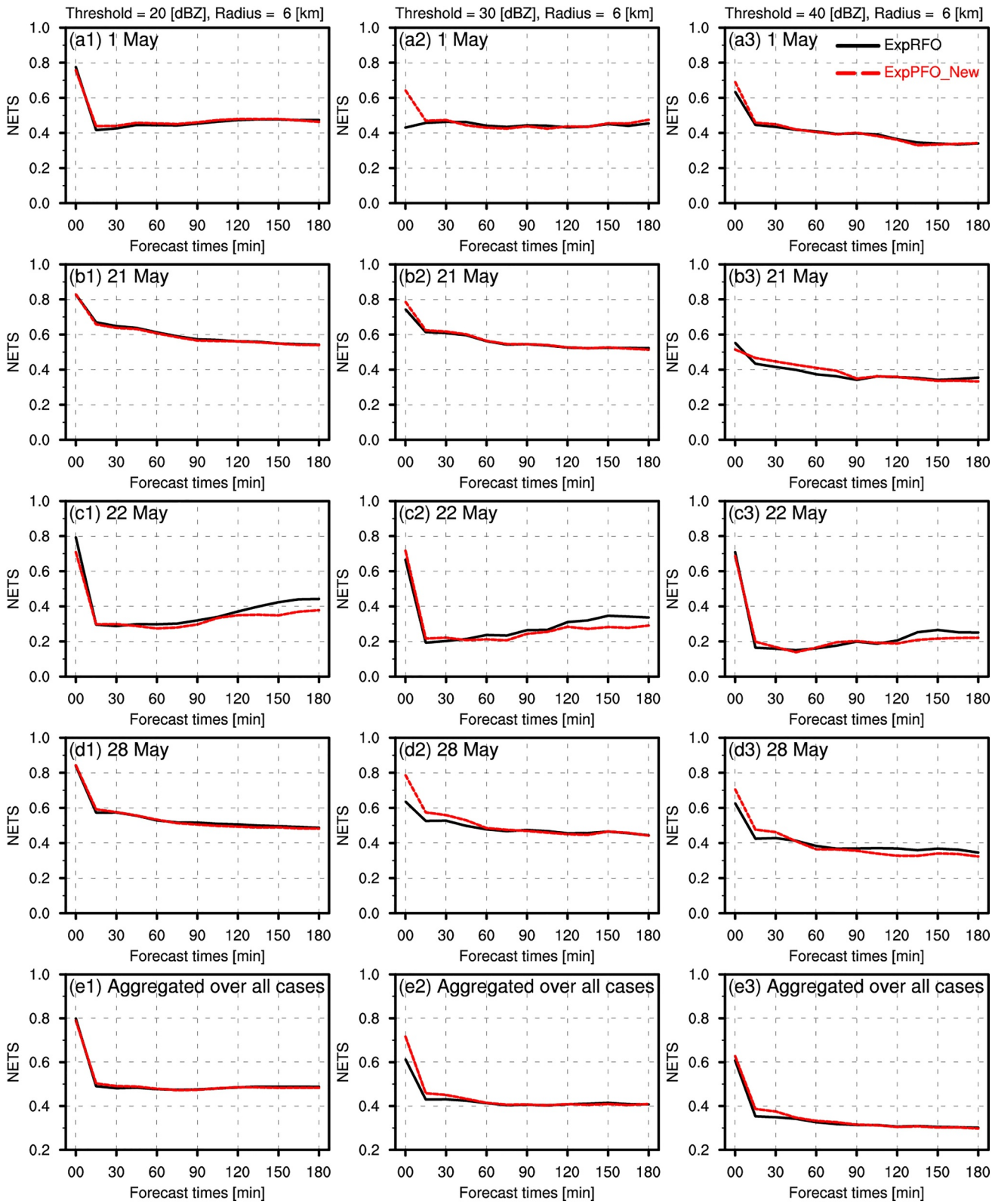

Figure 14. The Neighborhood Equitable Threat Score (NETS) with a 6-km radius of composite reflectivity forecasts for thresholds with 20 dBZ (a1–e1), 30 dBZ (a2–e2), and 40 dBZ (a3–e3). Panels (a1–a3), (b1–b3), (c1–c3), and (d1–d3) display the results averaged over four cycles from cases of 1 May, 21 May, 22 May, and 28 May 2019, respectively. Panels (e1–e3) display the result of aggregated over all eight cases. ExpRFO (black solid lines) and ExpPFO_New (red dashed lines) averaged over eight cases.

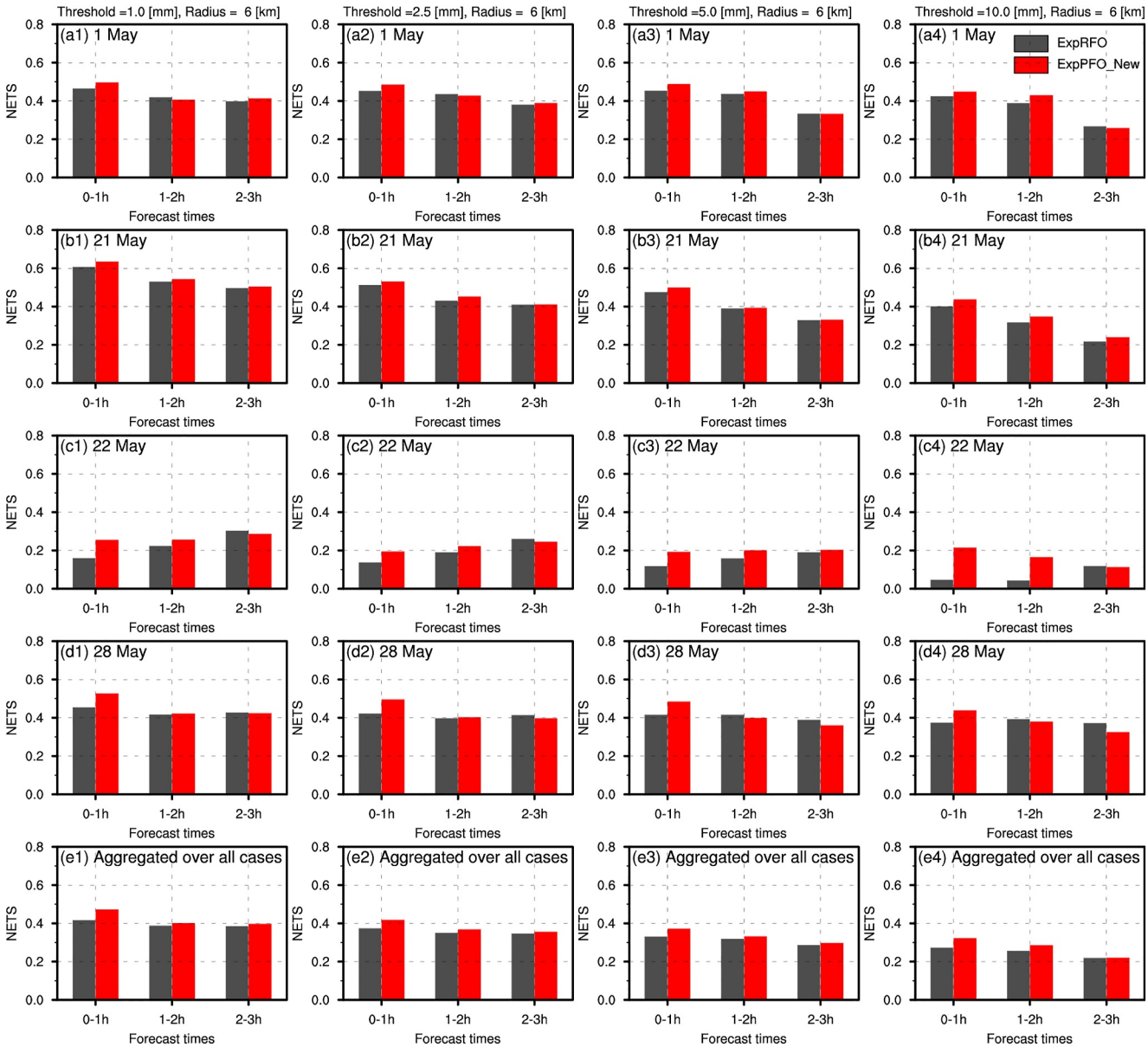

Figure 15. The Neighborhood Equitable Threat Score (NETS) with a 6-km radius of 1-hr accumulated precipitation forecasts for the threshold of 1.0 mm (a1–e1), 2.5 mm (a2–e2), 5.0 mm (a3–e3), and 10.0 mm (a4–e4). Panels (a1–a4), (b1–b4), (c1–c4), and (d1–d4) display the results averaged over four cycles from cases of 1 May, 21 May, 22 May, and 28 May 2019, respectively. Panels (e1–e4) display the result of aggregated over all eight cases. ExpRFO (black solid lines) and ExpPFO_New (red dashed lines) averaged over eight cases.

as well as mixed-phase particles. The continuous melting model used as part of the PFO characterizes melting mixed-phase species, addressing the limitation of microphysics schemes that include only rain and dry ice species.

The use of PFOs based on double-moment (DM) microphysics schemes in this study focuses on updating the mixing ratios of hydrometeors in the assimilation process. However, the full potential of this operator, which is capable of simulating and assimilating polarimetric radar variables, is not fully utilized. For example, updating the number concentrations of hydrometeors in the variational assimilation system is difficult and is not explored in this study. Doing this requires model variable transformations due to the large dynamic range of variations in number concentrations (Hu et al., 2023), though some research efforts, such as those involving the EnKF and ensemble-3DVAR assimilation systems, have already explored updating number concentrations (Li et al., 2022;

Zhu et al., 2020). Future studies will further evaluate the impact of using PFOs for updating both mixing ratios and number concentrations on analysis and forecasting. Moreover, the assimilation of dual-polarization radar data needs further exploration.

Data Availability Statement

For this work, the NEXRAD Level-II data used in this research can be accessed at the National Oceanic and Atmospheric Administration (NOAA) National Centers for Environmental Information website (http://www.ncei.noaa.gov; NOAA, 2015). More information about the NEXRAD radars can be found at https://www.ncei.noaa.gov/products/radar/next-generation-weather-radar. The Oklahoma Mesonet data (Brock et al., 1995) can be accessed at https://www.mesonet.org/index.php/past_data/mesonet_data_files. The Automated Surface/Weather Observing Systems (ASOS) data can be found at https://www.ncei.noaa.gov/products/land-based-station/automated-surface-weather-observing-systems. The WRF source code version 3.7.1 (Skamarock et al., 2008) is publicly available at NCAR/UCAR (https://github.com/wrf-model/WRF).

Acknowledgments
This work was supported by the NSF Grant 2136161. Funding was also provided by NOAA/Office of Oceanic and Atmospheric Research under NOAA-University of Oklahoma Cooperative Agreement NA21OAR4320204, U.S. Department of Commerce. The computing for this project was performed at the OU Supercomputing Center for Education and Research (OSCER) at the University of Oklahoma (OU) and the Anvil CPU at Purdue University through allocation EES220057 from the Advanced Cyberinfrastructure Coordination Ecosystem: Services and Support (ACCESS) program, which is supported by National Science Foundation Grants 2138259, 2138286, 2138307, 2137603, and 2138296.

References

Aksoy, A., Dowell, D. C., & Snyder, C. (2009). A multicase comparative assessment of the ensemble kalman filter for assimilation of radar observations. Part I: Storm-scale analyses. *Monthly Weather Review*, *137*(6), 1805–1824. https://doi.org/10.1175/2008MWR2691.1

Aksoy, A., Dowell, D. C., & Snyder, C. (2010). A multicase comparative assessment of the ensemble kalman filter for assimilation of radar observations. Part II: Short-range ensemble forecasts. *Monthly Weather Review*, *138*(4), 1273–1292. https://doi.org/10.1175/2009MWR3086.1

Auligné, T., Lorenc, A., Michel, Y., Montmerle, T., Jones, A., Hu, M., & Dudhia, J. (2011). Toward a new cloud analysis and prediction system. *Bulletin of the American Meteorological Society*, *92*(2), 207–210. https://doi.org/10.1175/2010BAMS2978.1

Bick, T., Simmer, C., Trömel, S., Wapler, K., Hendricks Franssen, H.-J., Stephan, K., et al. (2016). Assimilation of 3D radar reflectivities with an ensemble Kalman filter on the convective scale. *Quarterly Journal of the Royal Meteorological Society*, *142*(696), 1490–1504. https://doi.org/10.1002/qj.2751

Brock, F. V., Crawford, K. C., Elliott, R. L., Cuperus, G. W., Stadler, S. J., Johnson, H. L., & Eilts, M. D. (1995). The Oklahoma Mesonet: A technical overview [Dataset]. *Journal of Atmospheric and Oceanic Technology*, *12*(1), 5–19. https://doi.org/10.1175/1520-0426(1995)012<0005:TOMATO>2.0.CO;2

Carpenter, N. (2022). *Evaluation of the experimental warn-on-forecast system and WoF-hybrid 3DEnVar system on short-term forecasts for 2021 real-time cases* (p. 129). University of Oklahoma.

Chen, H., Gao, J., Wang, Y., Chen, Y., Sun, T., Carlin, J., & Zheng, Y. (2021). Radar reflectivity data assimilation method based on background-dependent hydrometeor retrieval: Comparison with direct assimilation for real cases. *Quarterly Journal of the Royal Meteorological Society*, *147*(737), 2409–2428. https://doi.org/10.1002/qj.4031

Clark, A. J., Gallus, W. A., & Weisman, M. L. (2010). Neighborhood-based verification of precipitation forecasts from convection-allowing NCAR WRF model simulations and the operational NAM. *Weather and Forecasting*, *25*(5), 1495–1509. https://doi.org/10.1175/2010WAF2222404.1

Clark, A. J., Jirak, I. L., Gallo, B. T., Roberts, B., Knopfmeier, K. H., Clark, R. A., et al. (2020). A real-time, simulated forecasting experiment for advancing the prediction of hazardous convective weather. *Bulletin of the American Meteorological Society*, *101*(11), E2022–E2024. https://doi.org/10.1175/BAMS-D-19-0298.1

Dowell, D. C., Alexander, C. R., James, E. P., Weygandt, S. S., Benjamin, S. G., Manikin, G. S., et al. (2022). The high-resolution Rapid Refresh (HRRR): An hourly updating convection-allowing forecast model. Part I: Motivation and system description. *Weather and Forecasting*, *37*(8), 1371–1395. https://doi.org/10.1175/WAF-D-21-0151.1

Dowell, D. C., Wicker, L. J., & Snyder, C. (2011). Ensemble kalman filter assimilation of radar observations of the 8 may 2003 Oklahoma City supercell: Influences of reflectivity observations on storm-scale analyses. *Monthly Weather Review*, *139*(1), 272–294. https://doi.org/10.1175/2010MWR3438.1

Du, M., Gao, J., Zhang, G., Wang, Y., Heiselman, P. L., & Cui, C. (2021). Assimilation of polarimetric radar data in simulation of a supercell storm with a variational approach and the WRF model. *Remote Sens-Basel*, *13*(16), 3060. https://doi.org/10.3390/rs13163060

Gan, R., Yang, Y., Qiu, X., Liu, P., Wang, X., & Gu, K. (2022). A scheme to suppress spurious convection by assimilating the "zero" column maximum vertical velocity. *Journal of Geophysical Research: Atmospheres*, *127*(4). https://doi.org/10.1029/2021jd035536

Gao, J. (2017). A three-dimensional variational radar data assimilation scheme developed for convective scale NWP. In S. K. Park & L. Xu (Eds.), *Data assimilation for atmospheric, oceanic and hydrologic applications* (Vol. III, pp. 285–326). Springer International Publishing. https://doi.org/10.1007/978-3-319-43415-5_13

Gao, J., and coauthors (2021). Testing of an experimental warn-on-forecast (WoF) hybrid data assimilation and forecasting system during the HWT spring experiment in 2019 and 2020, in *11th conference on transition of research to operations*. Retrieved from https://ams.confex.com/ams/101ANNUAL/meetingapp.cgi/Paper/382602

Gao, J., & Stensrud, D. J. (2012). Assimilation of reflectivity data in a convective-scale, cycled 3DVAR framework with hydrometeor classification. *Journal of the Atmospheric Sciences*, *69*(3), 1054–1065. https://doi.org/10.1175/JAS-D-11-0162.1

Gao, J., & Stensrud, D. J. (2014). Some observing system simulation experiments with a hybrid 3DEnVAR system for storm-scale radar data assimilation. *Monthly Weather Review*, *142*(9), 3326–3346. https://doi.org/10.1175/MWR-D-14-00025.1

Gao, J., Xue, M., Brewster, K., & Droegemeier, K. K. (2004). A three-dimensional variational data analysis method with recursive filter for Doppler radars. *Journal of Atmospheric and Oceanic Technology*, *21*(3), 457–469. https://doi.org/10.1175/1520-0426(2004)021<0457:ATVDAM>2.0.CO;2

Gao, J., Xue, M., Shapiro, A., & Droegemeier, K. K. (1999). A variational method for the analysis of three-dimensional wind fields from two Doppler radars. *Monthly Weather Review*, *127*(9), 2128–2142. https://doi.org/10.1175/1520-0493(1999)127<2128:AVMFTA>2.0.CO;2

Garnett, J. C. M. (1904). XII. Colours in metal glasses and in metallic films. *Philosophical Transactions of the Royal Society of London - Series A: Containing Papers of a Mathematical or Physical Character*, *203*(359–371), 385–420. https://doi.org/10.1098/rsta.1904.0024

Gastaldo, T., Poli, V., Marsigli, C., Cesari, D., Alberoni, P. P., & Paccagnella, T. (2021). Assimilation of radar reflectivity volumes in a pre-operational framework. *Quarterly Journal of the Royal Meteorological Society*, *147*(735), 1031–1054. https://doi.org/10.1002/qj.3957

Gilmore, M. S., Straka, J. M., & Rasmussen, E. N. (2004). Precipitation and evolution sensitivity in simulated deep convective storms: Comparisons between liquid-only and simple ice and liquid phase microphysics. *Monthly Weather Review*, *132*(8), 1897–1916. https://doi.org/10.1175/1520-0493(2004)132<1897:PAESIS>2.0.CO;2

Hong, S.-Y., Noh, Y., & Dudhia, J. (2006). A new vertical diffusion package with an explicit treatment of entrainment processes. *Monthly Weather Review*, *134*(9), 2318–2341. https://doi.org/10.1175/MWR3199.1

Hu, J., Gao, J., Liu, C., Zhang, G., Heinselman, P., & Carlin, J. T. (2023). Test of power transformation function to hydrometeor and water vapor mixing ratios for direct variational assimilation of radar reflectivity data. *Weather and Forecasting*, *38*(10), 1995–2010. https://doi.org/10.1175/WAF-D-22-0158.1

Hu, M., Xue, M., & Brewster, K. (2006). 3DVAR and cloud analysis with WSR-88D level-II data for the prediction of the fort worth, Texas, tornadic thunderstorms. Part I: Cloud analysis and its impact. *Monthly Weather Review*, *134*(2), 675–698. https://doi.org/10.1175/MWR3092.1

Iacono, M. J., Delamere, J. S., Mlawer, E. J., Shephard, M. W., Clough, S. A., & Collins, W. D. (2008). Radiative forcing by long-lived greenhouse gases: Calculations with the AER radiative transfer models. *Journal of Geophysical Research*, *113*(D13). https://doi.org/10.1029/2008JD009944

Jr Smith, P., Myers, C., & Orville, H. (1975). Radar reflectivity factor calculations in numerical cloud models using bulk parameterization of precipitation. *Journal of Applied Meteorology and Climatology*, *14*(6), 1156–1165. https://doi.org/10.1175/1520-0450(1975)014<1156:rrfcin>2.0.co;2

Jung, Y., Xue, M., & Zhang, G. (2010). Simulations of polarimetric radar signatures of a supercell storm using a two-moment bulk microphysics scheme. *Journal of Applied Meteorology and Climatology*, *49*(1), 146–163. https://doi.org/10.1175/2009jamc2178.1

Jung, Y., Zhang, G., & Xue, M. (2008). Assimilation of simulated polarimetric radar data for a convective storm using the ensemble kalman filter. Part I: Observation operators for reflectivity and polarimetric variables. *Monthly Weather Review*, *136*(6), 2228–2245. https://doi.org/10.1175/2007mwr2083.1

Li, H., Liu, C., Xue, M., Park, J., Chen, L., Jung, Y., et al. (2022). Use of power transform total number concentration as control variable for direct assimilation of radar reflectivity in GSI En3DVar and tests with six convective storms cases. *Monthly Weather Review*, *150*(4), 821–842. https://doi.org/10.1175/MWR-D-21-0041.1

Li, H., Sun, J., Yang, Y., Kong, X., & Gan, R. (2023). Effects of large-scale constraint and constraint variables on the high-frequency assimilation of radar reflectivity data in convective precipitation forecasting. *Climate Dynamics*, *61*(9), 4359–4375. https://doi.org/10.1007/s00382-023-06809-4

Lin, E., Yang, Y., Qiu, X., Xie, Q., Gan, R., Zhang, B., & Liu, X. (2021). Impacts of the radar data assimilation frequency and large-scale constraint on the short-term precipitation forecast of a severe convection case. *Atmospheric Research*, *257*, 105590. https://doi.org/10.1016/j.atmosres.2021.105590

Lin, Y.-L., Farley, R. D., & Orville, H. D. (1983). Bulk parameterization of the snow field in a cloud model. *Journal of Applied Meteorology and Climatology*, *22*(6), 1065–1092. https://doi.org/10.1175/1520-0450(1983)022<1065:BPOTSF>2.0.CO;2

Liu, C., Li, H., Xue, M., Jung, Y., Park, J., Chen, L., et al. (2022). Use of a reflectivity operator based on double-moment thompson microphysics for direct assimilation of radar reflectivity in GSI-based hybrid En3DVar. *Monthly Weather Review*, *150*(4), 907–926. https://doi.org/10.1175/MWR-D-21-0040.1

Liu, C., Xiao, Q., & Wang, B. (2008). An ensemble-based four-dimensional variational data assimilation scheme. Part I: Technical formulation and preliminary test. *Monthly Weather Review*, *136*(9), 3363–3373. https://doi.org/10.1175/2008MWR2312.1

Liu, P., Yang, Y., Lai, A., Wang, Y., Fierro, A. O., Gao, J., & Wang, C. (2021). Assimilating FY-4A lightning and radar data for improving short-term forecasts of a high-impact convective event with a dual-resolution hybrid 3DEnVAR method. *Remote Sens-Basel*, *13*(16), 3090. https://doi.org/10.3390/rs13163090

Liu, P., Zhang, G., Carlin, J. T., & Gao, J. (2024). A new melting model and its implementation in parameterized forward operators for polarimetric radar data simulation with double moment microphysics schemes. *Journal of Geophysical Research: Atmospheres*, *129*(9), e2023JD040026. https://doi.org/10.1029/2023JD040026

Mahale, V. N., Zhang, G., Xue, M., Gao, J., & Reeves, H. D. (2019). Variational retrieval of rain microphysics and related parameters from polarimetric radar data with a parameterized operator. *Journal of Atmospheric and Oceanic Technology*, *36*(12), 2483–2500. https://doi.org/10.1175/jtech-d-18-0212.1

Milbrandt, J., & Yau, M. (2005a). A multimoment bulk microphysics parameterization. Part I: Analysis of the role of the spectral shape parameter. *Journal of the Atmospheric Sciences*, *62*(9), 3051–3064. https://doi.org/10.1175/jas3534.1

Milbrandt, J., & Yau, M. (2005b). A multimoment bulk microphysics parameterization. Part II: A proposed three-moment closure and scheme description. *Journal of the Atmospheric Sciences*, *62*(9), 3065–3081. https://doi.org/10.1175/jas3535.1

National Oceanic and Atmospheric Administration (NOAA). (2015). The next generation weather radar (NEXRAD) level-II data [Dataset]. *National Centers for Environmental Information (NCEI)*. Retrieved from https://www.ncei.noaa.gov

Pan, S., Gao, J., Stensrud, D. J., Wang, X., & Jones, T. A. (2018). Assimilation of radar radial velocity and reflectivity, satellite cloud water path, and total precipitable water for convective-scale NWP in OSSEs. *Journal of Atmospheric and Oceanic Technology*, *35*(1), 67–89. https://doi.org/10.1175/jtech-d-17-0081.1

Park, J., Xue, M., & Liu, C. (2023). Implementation and testing of radar data assimilation capabilities within the joint effort for data assimilation integration framework with ensemble transformation kalman filter coupled with FV3-LAM model. *Geophysical Research Letters*, *50*(11), e2022GL102709. https://doi.org/10.1029/2022GL102709

Putnam, B., Jung, Y., Yussouf, N., Stratman, D., Supinie, T. A., Xue, M., et al. (2021). The impact of assimilating ZDR observations on storm-scale ensemble forecasts of the 31 may 2013 Oklahoma storm event. *Monthly Weather Review*, *149*(6), 1919–1942. https://doi.org/10.1175/MWR-D-20-0261.1

Putnam, B., Xue, M., Jung, Y., Snook, N., & Zhang, G. (2019). Ensemble kalman filter assimilation of polarimetric radar observations for the 20 may 2013 Oklahoma tornadic supercell case. *Monthly Weather Review*, *147*(7), 2511–2533. https://doi.org/10.1175/mwr-d-18-0251.1

Skamarock, W. C., Klemp, J. B., Dudhia, J., Gill, D. O., Barker, D. M., Duda, M. G., et al. (2008). A description of the advanced research WRF version 3 (No. NCAR/TN-475+STR) [Software], *475*, 113. https://doi.org/10.5065/D68S4MVH

Smith, P. L. (1984). Equivalent radar reflectivity factors for snow and ice particles. *Journal of Climate and Applied Meteorology*, *23*(8), 1258–1260. https://doi.org/10.1175/1520-0450(1984)023<1258:errffs>2.0.co;2

SPC. (2019). *SPC filtered storm reports for 5/24/2019*. NOAA/NWS/Storm Prediction Center. Retrieved from https://www.spc.noaa.gov/climo/reports/190524_rpts.html

Stephan, K., Klink, S., & Schraff, C. (2008). Assimilation of radar-derived rain rates into the convective-scale model COSMO-DE at DWD. *Quarterly Journal of the Royal Meteorological Society*, *134*(634), 1315–1326. https://doi.org/10.1002/qj.269

Sun, J., & Crook, N. A. (1997). Dynamical and microphysical retrieval from Doppler radar observations using a cloud model and its adjoint. Part I: Model development and simulated data experiments. *Journal of the Atmospheric Sciences*, *54*(12), 1642–1661. https://doi.org/10.1175/1520-0469(1997)054<1642:DAMRFD>2.0.CO;2

Sun, J., & Wang, H. (2013). Radar data assimilation with WRF 4D-Var. Part II: Comparison with 3D-Var for a squall line over the U.S. Great plains. *Monthly Weather Review*, *141*(7), 2245–2264. https://doi.org/10.1175/MWR-D-12-00169.1

Tong, C.-C., Jung, Y., Xue, M., & Liu, C. (2020). Direct assimilation of radar data with ensemble kalman filter and hybrid ensemble-variational method in the national weather service operational data assimilation system GSI for the stand-alone regional FV3 model at a convection-allowing resolution. *Geophysical Research Letters*, *47*(19), e2020GL090179. https://doi.org/10.1029/2020GL090179

Tong, M., & Xue, M. (2005). Ensemble kalman filter assimilation of Doppler radar data with a compressible nonhydrostatic model: OSS experiments. *Monthly Weather Review*, *133*(7), 1789–1807. https://doi.org/10.1175/MWR2898.1

Wang, H., Sun, J., Fan, S., & Huang, X.-Y. (2013). Indirect assimilation of radar reflectivity with WRF 3D-Var and its impact on prediction of four summertime convective events. *Journal of Applied Meteorology and Climatology*, *52*(4), 889–902. https://doi.org/10.1175/JAMC-D-12-0120.1

Wang, H., Sun, J., Zhang, X., Huang, X.-Y., & Auligné, T. (2013). Radar data assimilation with WRF 4D-Var. Part I: System development and preliminary testing. *Monthly Weather Review*, *141*(7), 2224–2244. https://doi.org/10.1175/MWR-D-12-00168.1

Wang, S., & Liu, Z. (2019). A radar reflectivity operator with ice-phase hydrometeors for variational data assimilation (version 1.0) and its evaluation with real radar data. *Geoscientific Model Development*, *12*(9), 4031–4051. https://doi.org/10.5194/gmd-12-4031-2019

Xiao, Q., Kuo, Y.-H., Sun, J., Lee, W.-C., Barker, D. M., & Lim, E. (2007). An approach of radar reflectivity data assimilation and its assessment with the inland QPF of typhoon rusa (2002) at landfall. *Journal of Applied Meteorology and Climatology*, *46*(1), 14–22. https://doi.org/10.1175/JAM2439.1

Xiao, Q., & Sun, J. (2007). Multiple-radar data assimilation and short-range quantitative precipitation forecasting of a squall line observed during IHOP_2002. *Monthly Weather Review*, *135*(10), 3381–3404. https://doi.org/10.1175/MWR3471.1

Yang, R., Purser, R. J., Carley, J. R., Pondeca, M., Zhu, Y., & Levine, S. (2020). *Application of a nonlinear transformation function to the variational analysis of visibility and ceiling height*, U.S. Department of commerce National Oceanic and Atmospheric Admiinistration.

Yang, Y., Qiu, C., & Gong, J. (2006). Physical initialization applied in WRF-Var for assimilation of Doppler radar data. *Geophysical Research Letters*, *33*(22). https://doi.org/10.1029/2006GL027656

Yussouf, N., Mansell, E. R., Wicker, L. J., Wheatley, D. M., & Stensrud, D. J. (2013). The ensemble kalman filter analyses and forecasts of the 8 may 2003 Oklahoma City tornadic supercell storm using single- and double-moment microphysics schemes. *Monthly Weather Review*, *141*(10), 3388–3412. https://doi.org/10.1175/MWR-D-12-00237.1

Zeng, Y., Blahak, U., & Jerger, D. (2016). An efficient modular volume-scanning radar forward operator for NWP models: Description and coupling to the COSMO model. *Quarterly Journal of the Royal Meteorological Society*, *142*(701), 3234–3256. https://doi.org/10.1002/qj.2904

Zhang, F., Snyder, C., & Sun, J. (2004). Impacts of initial estimate and observation availability on convective-scale data assimilation with an ensemble kalman filter. *Monthly Weather Review*, *132*(5), 1238–1253. https://doi.org/10.1175/1520-0493(2004)132<1238:IOIEAO>2.0.CO;2

Zhang, G. (2016). *Weather radar polarimetry*. CRC Press.

Zhang, G., Gao, J., & Du, M. (2021). Parameterized forward operators for simulation and assimilation of polarimetric radar data with numerical weather predictions. *Advances in Atmospheric Sciences*, *38*(5), 737–754. https://doi.org/10.1007/s00376-021-0289-6

Zhu, K., Xue, M., Ouyang, K., & Jung, Y. (2020). Assimilating polarimetric radar data with an ensemble kalman filter: OSSEs with a tornadic supercell storm simulated with a two-moment microphysics scheme. *Quarterly Journal of the Royal Meteorological Society*, *146*(729), 1880–1900. https://doi.org/10.1002/qj.3772